

Forces on Dust Grains Exposed to Anisotropic Interstellar Radiation Fields

Joseph C. Weingartner

Physics Dept., Jadwin Hall, Princeton University, Princeton, NJ 08544, USA; CITA, 60 St. George Street, University of Toronto, Toronto, ON M5S 3H8, Canada

weingart@cita.utoronto.ca

and

B.T. Draine

Princeton University Observatory, Peyton Hall, Princeton, NJ 08544, USA

draine@astro.princeton.edu

ABSTRACT

Grains exposed to anisotropic radiation fields are subjected to forces due to the asymmetric photon-stimulated ejection of particles. These forces act in addition to the “radiation pressure” due to absorption and scattering. Here we model the forces due to photoelectron emission and the photodesorption of atoms. The “photoelectric” force depends on the ambient conditions relevant to grain charging. We find that it is comparable to the radiation pressure when the grain potential is relatively low and the radiation spectrum is relatively hard. The calculation of the “photodesorption” force is highly uncertain, since the surface physics and chemistry of grain materials are poorly understood at present. For our simple yet plausible model, the photodesorption force dominates the radiation pressure for grains larger than $\sim 0.1\mu\text{m}$ exposed to starlight from OB stars. We find that the anisotropy of the interstellar radiation field is $\sim 10\%$ in the visible and ultraviolet. We estimate size-dependent drift speeds for grains in the cold and warm neutral media and find that micron-sized grains could potentially be moved across a diffuse cloud during its lifetime.

Subject headings: dust

1. Introduction

Anisotropic radiation fields are common in the interstellar medium (ISM). Of course, the radiation is highly anisotropic at points located close to a star or cluster or at the edge of a molecular cloud. These include the astronomically important photodissociation regions (PDRs), the surface layers of molecular clouds, where incident UV dissociates molecules. The visible/UV

radiation field in the diffuse ISM is due primarily to starlight; since stars are unevenly distributed, it too is anisotropic. Dust grains in this radiation field are subjected to torques, if their shapes are somewhat asymmetric, and this may be responsible for the alignment of interstellar grains (Draine & Weingartner 1996, 1997), which is inferred from the observed polarization of starlight (Hiltner 1949a, b; Hall 1949; Hall & Mikesell 1949).

Grains exposed to anisotropic radiation are subjected to forces as well as to torques, again with potentially important consequences. If the “radiative” forces are large enough to result in substantial gas-grain drift, then this could lead to spatial variation in the dust-to-gas ratio. If the drift depends on grain size, then grain coagulation could result. Here we investigate two potentially significant forces, due to the recoil associated with electrons and adsorbed H atoms, which are ejected from the grain with some non-zero probability following photon absorption.

Lafon (1990) modeled the net force due to anisotropic photoelectron emission for grains exposed to unidirectional radiation fields and found that, for some interstellar conditions, it substantially exceeds the radiation pressure, due to absorption and scattering. Lafon considered spherical grains and assumed that electrons are emitted only from the illuminated hemisphere. However, interstellar grain radii can be smaller than the photon attenuation length, so that electrons are also emitted from the non-illuminated hemisphere. In §3, we revisit the calculation of photoelectric recoil forces on dust grains, employing the prescription of Kerker & Wang (1982) for estimating the anisotropy in photoelectron momentum.

In §4, we consider the force due to the anisotropic photodesorption of adsorbed H atoms. An atom starts out in the gas phase, collides with and sticks to the grain surface, and can be removed when an absorbed photon breaks its bond to the surface. Of course, there are many other grain surface processes, besides adsorption and photodesorption, and these too could play important roles in determining the emission anisotropy. Since interstellar grains have not yet been well characterized, the details of their surface physics are unknown. We adopt a simple, yet plausible, model and evaluate the “photodesorption” force for this one case.

Following the investigations of the photoelectric and photodesorption forces, we discuss, in §5, how surface processes can affect the drag force experienced by drifting grains. In §6, we estimate the anisotropy of the interstellar radiation field. In §7, we estimate drift speeds for grains in the diffuse ISM, tying together the results from the previous sections. In a separate paper (Weingartner & Draine 2001c), we will investigate gas-grain drift in PDRs.

2. Radiation Pressure Force

We generally normalize our results for the “photoelectric” and “photodesorption” forces to the radiation pressure force, in order to see whether or not they are significant. The force due to radiation pressure is

$$F_{\text{rad}} = \pi a^2 \langle Q_{\text{pr}} \rangle \Delta u_{\text{rad}} \quad , \quad (1)$$

where a is the grain radius (we assume spherical grains in all of our calculations) and $c\Delta u_{\text{rad}}$ is the net energy flux in the radiation field ($\Delta u_{\text{rad}} = u_{\text{rad}}$, the total energy density, for a unidirectional radiation field and $\Delta u_{\text{rad}} = 0$ for an isotropic radiation field). The spectrum-averaged radiation pressure efficiency factor is given by

$$\langle Q_{\text{pr}} \rangle \equiv \frac{\int_0^{\nu_{\text{max}}} [Q_{\text{abs}} + Q_{\text{sca}}(1 - \langle \cos \theta \rangle)] u_{\nu} d\nu}{\int_0^{\nu_{\text{max}}} u_{\nu} d\nu}, \quad (2)$$

where $Q_{\text{abs}}\pi a^2$ is the absorption cross section, $Q_{\text{sca}}\pi a^2$ is the scattering cross section, $\langle \cos \theta \rangle$ is the usual scattering asymmetry factor, and ν_{max} is the highest frequency in the radiation field. We will take $h\nu_{\text{max}} = 13.6 \text{ eV}$, because H I regions are highly opaque to H-ionizing radiation. We evaluate Q_{abs} , Q_{sca} , and $\langle \cos \theta \rangle$ using a Mie theory code derived from BHMIE (Bohren & Huffman 1983). We consider carbonaceous and silicate compositions and take optical properties from Draine & Lee (1984), Laor & Draine (1993), and Li & Draine (2001), as described by Weingartner & Draine (2001a).

We consider two types of radiation spectrum. To characterize regions located near a single star, we adopt a blackbody spectrum (cut off at 13.6 eV), with color temperature T_c and dilution factor W , so that the energy density per unit frequency interval $u_{\nu} = 4\pi W B_{\nu}(T_c)/c$. It is convenient to characterize the radiation intensity by $G \equiv u_{\text{rad}}^{\text{uv}}/u_{\text{Hab}}^{\text{uv}}$, where $u_{\text{rad}}^{\text{uv}}$ is the energy density in the radiation field between 6 eV and 13.6 eV and $u_{\text{Hab}}^{\text{uv}} = 5.33 \times 10^{-14} \text{ erg cm}^{-3}$ is the Habing (1968) estimate of the starlight energy density in this range.¹

For the diffuse ISM, we adopt the average interstellar radiation field (ISRF) spectrum in the solar neighborhood, as estimated by Mezger, Mathis, & Panagia (1982) and Mathis, Mezger, & Panagia (1983); see Weingartner & Draine (2001b) for a convenient representation of the ISRF. The total energy density in the ISRF is $u = 8.64 \times 10^{-13} \text{ erg cm}^{-3}$, with $u_{\text{rad}}^{\text{uv}} = 6.07 \times 10^{-14} \text{ erg cm}^{-3}$ in the 6-13.6 eV interval, or $G = 1.13$.

In Figure 1 we display $\langle Q_{\text{pr}} \rangle$, as a function of grain size a , for the ISRF and blackbody spectra with various values of T_c . We consider grains with a as large as $1 \mu\text{m}$, even though the classic MRN size distribution (Mathis, Rumpl, & Nordsieck 1977) only extends up to $a = 0.25 \mu\text{m}$. The size distributions of Weingartner & Draine (2001a) contain non-negligible amounts of mass in grains with $a \sim 1 \mu\text{m}$, and we will find that the radiative forces are relatively large for such grains; thus, they could be important in some interstellar environments. We consider grains as small as $a = 10 \text{ \AA}$, equal to the value adopted by Weingartner & Draine (2001b) for the electron escape length, the typical distance that an excited electron travels within a grain before losing its energy. This choice is somewhat arbitrary, but this does not matter, since the radiative forces are inconsequential for grains with $a \sim 10 \text{ \AA}$.

¹For comparison, the interstellar radiation field estimated by Draine (1978) has $u = 8.93 \times 10^{-14} \text{ erg cm}^{-3}$ between 6 and 13.6 eV, or $G = 1.68$.

3. “Photoelectric” Force

3.1. Model

We adopt the photoemission model of Weingartner & Draine (2001b). The photoemission rate and photoelectron energy both depend on the grain charge, so it is necessary to evaluate the charge distribution $f_Z(a)$ = the probability that the grain has charge Ze , where e is the proton charge. The charge distribution is set primarily by a balance between electron loss via photoemission and gain via accretion from the gas. Charging by this process is determined mainly by the parameter $G\sqrt{T}/n_e$ (T is the gas temperature and n_e is the electron density), with an additional mild dependence on T (Bakes & Tielens 1994; Weingartner & Draine 2001b).

The photoelectric force on a grain is given by

$$F_{\text{pe}}(a) = \sum_Z f_Z(a) [F_{\text{pe,v}}(a, Z) + F_{\text{pe,a}}(a, Z)] \quad , \quad (3)$$

where $F_{\text{pe,v}}(a, Z)$ is the force due to electrons emitted from the valence band. When $Z < 0$, the $-Z$ “attached” electrons occupy energy levels above the valence band, if the latter is full in the neutral; $F_{\text{pe,a}}(a, Z)$ is the force due to the emission of these attached electrons.

The contribution from the photoemission of valence electrons is

$$F_{\text{pe,v}}(a, Z) = \pi a^2 \int_{\nu_{\text{pet}}}^{\nu_{\text{max}}} d\nu AYQ_{\text{abs}} \frac{c u_\nu}{h\nu} \sqrt{2m_e} \int_{E_{\text{min}}}^{E_{\text{max}}} dE f_E(E) \sqrt{E} S(Z, a, E) \quad , \quad (4)$$

where the photoemission threshold energy $h\nu_{\text{pet}}$ is the minimum energy that an absorbed photon must have for an electron to be ejected from the valence band, E_{min} (E_{max}) is the minimum (maximum) photoelectron kinetic energy (at infinity), and $f_E(E)$ is the photoelectron kinetic energy (at infinity) distribution; see Weingartner & Draine (2001b) for prescriptions for evaluating these quantities. The emission asymmetry factor $A(h\nu, a)$ measures the asymmetry in the emission of photoelectrons over the grain surface, the recoil suppression factor $S(Z, a, E)$ accounts for electron emission in directions other than the surface normal, and m_e is the electron mass.

When $Z < 0$, the contribution from photodetachment is given by

$$F_{\text{pe,a}}(a, Z) = \int_{\nu_{\text{pdt}}}^{\nu_{\text{max}}} d\nu A \sigma_{\text{pdt}}(\nu) \frac{c u_\nu}{h\nu} \sqrt{2m_e(h\nu - h\nu_{\text{pdt}} + E_{\text{min}})} S(Z, a, E = h\nu - h\nu_{\text{pdt}} + E_{\text{min}}) \quad , \quad (5)$$

where the photodetachment threshold energy $h\nu_{\text{pdt}}$ is the minimum energy that an absorbed photon must have for an attached electron to be emitted from the grain and $\sigma_{\text{pdt}}(\nu)$ is the photodetachment cross section.

We follow the simple prescription of Kerker & Wang (1982) for estimating A . The probability of photoemission from any site on the surface is taken to be proportional to the electric intensity

$|\mathbf{E}|^2$ just below the surface at that point. Thus,

$$A(h\nu, a) = \frac{-\int_0^\pi \sin \theta \cos \theta |\mathbf{E}(\theta)|^2 d\theta}{\int_0^\pi \sin \theta |\mathbf{E}(\theta)|^2 d\theta} \quad , \quad (6)$$

where θ is the polar angle with respect to the direction of the incident radiation. The electric field $\mathbf{E}(\theta)$ is evaluated using Mie theory (Bohren & Huffman 1983).² In Figures 2 and 3 we display the asymmetry factor $A(h\nu, a)$ for grains exposed to unidirectional radiation fields as a function of incident photon energy for various grain sizes for carbonaceous and silicate composition, respectively. Generally, $A(h\nu, a)$ equals the value for a unidirectional field times $\Delta u_{\text{rad}}/u_{\text{rad}}$. Curiously, $A < 0$ for some values of $(h\nu, a)$.

We assume that the electrons emerge symmetrically with respect to the local surface normal, with a “cosine-law” angular distribution (i.e. the emission rate at angle ψ with respect to the surface normal $\propto \sin \psi \cos \psi d\psi$). For an uncharged grain, this would imply $S = 2/3$. When the grain is charged, the electron escapes on a hyperbolic trajectory, so that when it is at infinity its velocity vector makes an angle ψ_∞ with respect to the surface normal which differs from the corresponding angle at the surface, ψ . Taking this into account, we find

$$\begin{aligned} S &\equiv \frac{\int_0^{\pi/2} d\psi \sin \psi \cos \psi \cos \psi_\infty}{\int_0^{\pi/2} d\psi \sin \psi \cos \psi} \\ &= \frac{2}{3} \sqrt{1+b} - \frac{b}{2} + \frac{b^2(1+b/2)}{2(1+b)} \left[\ln \left| 1 + \frac{2}{b} \right| + \frac{1}{2} \ln \left(\frac{1+b/2 - \sqrt{1+b}}{1+b/2 + \sqrt{1+b}} \right) \right] + \frac{b^2}{2\sqrt{1+b}} \quad , \quad (7) \end{aligned}$$

$$b \equiv \frac{(Z+1)e^2}{aE} \quad , \quad (8)$$

where Ze is the grain charge prior to photoelectron emission. For $-1 \leq b \leq 10^4$, the simpler expression

$$S \approx \frac{1.107}{0.4669 + (b + 1.421)^{0.5043}} \quad (9)$$

is accurate to within 0.6%; we adopt this expression in our computations. When an electron tunnels across the Coulomb barrier of a negatively charged grain, $b < -1$ and the above classical derivation fails, since the grain surface is a classically forbidden location. We simply take $S = 1$ when $b < -1$.

3.2. Computational Results

The photoelectric force depends on the grain charge distribution, and hence on the parameters $G\sqrt{T}/n_e$ and T . In Figures 4 and 5, F_{pe} is plotted for carbonaceous and silicate grains, respectively, for $T = 10^2$ and 10^3 K and three values of $G\sqrt{T}/n_e$, ranging from 10^3 to $10^5 \text{ K}^{1/2} \text{ cm}^3$. For these

²We adopt dielectric functions as in Weingartner & Draine (2001b).

cases, we adopt a blackbody spectrum with $T_c = 3 \times 10^4$ K, cut off at 13.6 eV. We also provide results for conditions appropriate for the cold neutral medium (ISRF, $T = 100$ K, $n_e = 0.03 \text{ cm}^{-3}$, $G\sqrt{T}/n_e = 380$) and the warm neutral medium (ISRF, $T = 6000$ K, $n_e = 0.03 \text{ cm}^{-3}$, $G\sqrt{T}/n_e = 2900$).

Note that for a given value of $G\sqrt{T}/n_e$, the results do not change much as the temperature increases from 10^2 to 10^3 K. Also, $F_{\text{pe}}/F_{\text{rad}}$ decreases for higher $G\sqrt{T}/n_e$ because the higher ionization potentials quench the photoemission.

For the truncated blackbody spectrum, there is no systematic increase or decrease of $F_{\text{pe}}/F_{\text{rad}}$ over the full range of grain sizes, because the increase in the anisotropy of emitted electrons with grain size roughly compensates for the decrease in photoelectric yield. The sharp minimum near 300 Å in Figure 4 results from a local plateau in the variation of the anisotropy with grain size, which lies near the maximum of F_{rad} . For the ISRF, the photoelectric force becomes less important, compared with the radiation pressure, as the grain size increases beyond ~ 200 Å. As seen in Figure 1, for the relatively soft ISRF, the radiation pressure increases rapidly as a increases from 10 Å to 1 μm. The total energy density between 0 and 13.6 eV is about an order of magnitude greater for the ISRF than for a blackbody with $T_c = 3 \times 10^4$ K and $G = 1$. For $a = 10$ Å, F_{rad} is comparable for the two spectra, but is about an order of magnitude larger for the ISRF when $a = 1 \mu\text{m}$. Since $G = 1.13$ for the ISRF, F_{pe} is comparable for the two spectra.

In Figure 6 we show the effect of varying T_c over a range from 2×10^4 to 5×10^4 K, characteristic of hot stars, using carbonaceous grains and $G\sqrt{T}/n_e = 10^3 \text{ K}^{1/2} \text{ cm}^3$, $T = 100$ K as an example.

4. “Photodesorption” Force

4.1. Introduction and Model

In the process of adsorption, gas-phase atoms or molecules collide with and stick to a solid surface, forming either a weak van der Waals bond (physisorption) or a stronger chemical bond (chemisorption). Adsorbed atoms can be removed from interstellar grains by various desorption processes: 1) thermal desorption, in which a thermal fluctuation in the grain breaks the adsorption bond, 2) photodesorption, in which an absorbed photon breaks the bond, and 3) exothermic chemical reaction between two adatoms. If photodesorption is important, we expect a non-zero net recoil force in an anisotropic radiation field.

The details of adsorption on grain surfaces are poorly known at present. In particular, it is unclear whether adsorbed hydrogen atoms can diffuse across the surface, either by thermal barrier hopping or quantum mechanical tunneling. In their classic study of H₂ formation on grains, Hollenbach & Salpeter (1971) assumed that H physisorbs with binding energy ~ 0.03 eV, implying high mobility. Physisorption occurs on ice surfaces, so that this description is likely valid deep inside molecular clouds, where grains are covered with ice mantles. However, grain temperatures in

PDRs are high enough that any ice mantles have sublimed, and ice features (e.g. at $3.1\mu\text{m}$ for H_2O ice) are not observed in the extinction curves for the diffuse ISM. Tielens & Allamandola (1987) discuss experimental evidence that H chemisorbs on graphite and amorphous silicate surfaces, with binding energy in the 1–2 eV range. Also, theoretical studies (Mendoza & Ruetter 1989; Fromherz, Mendoza, & Ruetter 1993) of H adsorption on graphite find chemisorption with binding energies in this range. For such large binding energies, thermal diffusion is negligible. The tunneling rate is approximately given by the oscillation frequency of the atom in the chemisorption potential times the barrier penetration factor, so that

$$\tau_t \sim 10^{-13} \text{ s} \exp \left[\frac{2d}{\hbar} (2mE_b)^{1/2} \right] , \quad (10)$$

where τ_t is the tunneling timescale, d is the distance between binding sites, m is the mass of the adatom, and E_b is the binding energy. The argument of the exponential is a large number; if $(E_b, d) = (1 \text{ eV}, 1 \text{ \AA})$, then $\tau_t \sim 13$ days for H adatoms. If d is increased to 2 \AA , then $\tau_t \sim 4 \times 10^{17}$ years. We assume that no diffusion occurs, primarily because this case is easier to model. Once a binding site is occupied by a chemisorbed H atom, another H can physisorb on top of the first (Tielens & Allamandola 1987). An atom in such a physisorption state can easily migrate to neighboring sites; also, if it can overcome an activation energy, it can react with the underlying H atom.

In our model, we assume that each surface site is a chemisorption site, from which adatoms cannot diffuse. For simplicity, we also ignore gas-phase species other than H. When an H atom from the gas arrives at an empty site, it sticks with probability s_H ; otherwise it is assumed to undergo perfectly elastic specular reflection. Since the binding energy in the chemisorption site greatly exceeds the kinetic energies of the atoms in the gas, we take $s_H = 1$. Also, we make the simplifying assumption that an H atom arriving at an occupied site either combines with the resident chemisorbed atom, with probability s_c , or else undergoes elastic specular reflection. This approximation is most reasonable for high gas temperatures, when the kinetic energies of the gas-phase atoms exceed the physisorption energy and reaction activation barrier. We also assume that H_2 molecules leave the grain immediately upon formation.

To calculate the net force on a grain we must evaluate, as a function of location on the grain surface, the average rate at which momentum is transferred to the grain per surface site. Momentum transfer occurs when an atom is photodesorbed, a newly-formed molecule leaves the grain, a gas-phase atom reflects off of the grain, or a gas-phase atom sticks to the grain (either at an unoccupied site, where it remains until it is removed by photodesorption or molecule formation, or at an occupied site, where it immediately forms a molecule, which leaves the grain).

We denote the rate at which gas phase H atoms arrive at a site by R_{arr} . The rate at which incident H sticks per empty site is given by $s_H R_{\text{arr}}$ and the rate at which H_2 is formed per occupied site is given by $s_c R_{\text{arr}}$. When a grain drifts with respect to the gas the arrival rate R_{arr} varies over the grain surface; of course, this results in the drag force. Baines, Williams, & Asebiomo (1965) calculated the drag, assuming that all arriving atoms undergo specular reflection. The surface processes considered here substantially complicate the drag calculation and the variable

R_{arr} complicates the net force due to photodesorptions. We will call the net force on a non-drifting grain, due to all of the processes mentioned above, the “photodesorption” force. In §5 we will discuss how the drag force is modified when the surface processes are taken into account.

4.2. Photodesorption Rate

The rate at which H is photodesorbed per occupied site is denoted by $R_{\text{pd}} = R_{\text{pd}}^0 \Psi(\theta')$, where R_{pd}^0 is the photodesorption rate averaged over the grain surface (\approx the incident photon flux density times the photodesorption cross section) and $\Psi(\theta')$ describes the variation in photodesorption rate as a function of the angle θ' with respect to the direction $\hat{\mathbf{S}}$ of net energy flux.

The photodesorption cross sections are not known. There is a substantial literature on experimentally determined cross sections for simple molecules on a variety of substrates, which is summarized in the review by Franchy (1998). For example, for NO and photon energies ~ 6 eV or less, the cross sections range from $\sim 10^{-22}$ cm² to 2×10^{-17} cm². The cross section increases with progression through the following sequence of substrates: platinum metals, noble metals, semiconductors, oxides. The differences are due to variation in the efficiency with which the substrates quench the excited states.

Hellsing et al. (1997) studied the photodesorption of K from graphite for photon energies ≤ 5 eV and found a maximum cross section of $\approx 2 \times 10^{-20}$ cm². However, for these photon energies the desorption is substrate-induced. That is, a bulk excitation (e.g. a photoelectron) travels to the adsorbed atom and excites it.

Photons with adequately high energy can directly excite the adsorbed atoms. We estimate the photodesorption cross sections due to this direct process, for H on graphite and silicates, by considering the photodissociation of the CH and OH molecules. Photodissociation cross sections for CH and OH have been calculated by van Dishoeck (1987) and van Dishoeck & Dalgarno (1984), respectively. The cross sections reach values as high as a few $\times 10^{-17}$ cm², and are appreciable for photon energies ≥ 6 eV. Roberge et al. (1991) found photodissociation rates of 8.6×10^{-10} s⁻¹ and 3.5×10^{-10} s⁻¹ for CH and OH, respectively, for the Draine (1978) radiation field. In the absence of more relevant experimental evidence, we simply set the photodesorption rates equal to the photodissociation rates. Also, in our crude approximation, we ignore variations in the shape of the radiation spectrum, and simply take the photodesorption rate proportional to $u_{\text{rad}}^{\text{UV}}$, the total energy density between 6 and 13.6 eV. Since $G = 1.68$ for the Draine radiation field, we take $R_{\text{pd}}^0 = 5 \times 10^{-10} G \text{ s}^{-1}$ for carbonaceous grains and $R_{\text{pd}}^0 = 2 \times 10^{-10} G \text{ s}^{-1}$ for silicates.

To evaluate $\Psi(\theta')$ we assume that, for any point on the grain surface, R_{pd} is proportional to the electric intensity $|\mathbf{E}_e|^2$ just above the surface at that point. Thus,

$$\Psi(\theta') = \frac{2 \int_{6 \text{ eV}/h}^{13.6 \text{ eV}/h} d\nu u_\nu |\mathbf{E}_e(\theta')|^2}{\int_0^\pi d\xi \sin \xi \int_{6 \text{ eV}/h}^{13.6 \text{ eV}/h} d\nu u_\nu |\mathbf{E}_e(\xi)|^2} . \quad (11)$$

In Figures 7 and 8, we display $\Psi(\theta')$ for carbonaceous and silicate grains, respectively, for a unidirectional radiation field and several values of grain radius a . Here we assume a blackbody spectrum (cut off at 13.6 eV) with $T_c = 3 \times 10^4$ K. For $a < 100$ Å, $\Psi(\theta')$ looks like the 100 Å curve, with greater symmetry for smaller grains. Generally,

$$\Psi(\theta') = \frac{(u_{\text{rad}} - \Delta u_{\text{rad}}) + \Delta u_{\text{rad}} \Psi^0(\theta')}{u_{\text{rad}}} \quad , \quad (12)$$

where $\Psi^0(\theta')$ is the value for a unidirectional field.

4.3. Surface Site Occupation Fraction

The momentum transfer rates depend on the occupation fraction f , i.e. the fraction of the time that a site is occupied by an H atom. If the grain's surface is fixed with respect to the radiation, then f is a function of the angle θ' with respect to $\hat{\mathbf{S}}$. However, the polarization of starlight implies that grains spin, with their spin axes statistically aligned (presumably with the magnetic field). Purcell (1979) noted that systematic torques likely act on grains, resulting in rotational speeds orders of magnitude greater than what would be expected from equipartition arguments. The spin period is much shorter than the timescales on which the surface processes occur, so that f is a function of the angle θ with respect to the spin axis $\hat{\boldsymbol{\omega}}$.

We evaluate $f(\theta)$ by balancing the the rate at which H is removed from an occupied site by photodesorption and H₂ formation against the rate at which H is added to an empty site when arriving gas-phase atoms stick:

$$f (\bar{R}_{\text{pd}} + s_c \bar{R}_{\text{arr}}) = (1 - f) s_{\text{H}} \bar{R}_{\text{arr}} \quad , \quad (13)$$

where bars denote averaging over the spin. This yields

$$f(\theta) = s_{\text{H}} [s_{\text{H}} + s_c + \alpha \bar{\Psi}(\theta)]^{-1} \quad . \quad (14)$$

The parameter α is defined by

$$\alpha \equiv \frac{R_{\text{pd}}^0}{R_{\text{arr}}^0} \quad , \quad (15)$$

where the H arrival rate for a non-drifting grain is given by

$$R_{\text{arr}}^0 = \frac{1}{2} n_{\text{H}} l^2 (\pi \beta)^{-1/2} \quad ; \quad (16)$$

n_{H} is the H number density, l^2 is the area of a surface site, and $\beta = m_p/2kT$. Of course,

$$\bar{\Psi}(\theta) = \frac{1}{2\pi} \int_0^{2\pi} d\phi \Psi(\theta') \quad , \quad (17)$$

where ϕ is the azimuthal angle about $\hat{\boldsymbol{\omega}}$.

Lazarian & Draine (1999a,b) have recently suggested that grains sometimes undergo rapid “flipping” of the principal axis of largest moment of inertia (fixed in body coordinates), alternating between being parallel or antiparallel to the angular momentum vector. We consider the limit where flips occur instantaneously, so that

$$f(\theta) = s_H \left\{ s_H + s_c + \frac{\alpha}{2} [\bar{\Psi}(\theta) + \bar{\Psi}(\pi - \theta)] \right\}^{-1} . \quad (18)$$

Although rapid flipping does not seem likely for suprathermally rotating grains with $a \gtrsim 0.1 \mu\text{m}$ (because of the large energy barrier that must be overcome in order to flip), the calculation of the photodesorption force in this case is instructive. Thus, we will consider both flipping and non-flipping grains.

4.4. Evaluation of the Photodesorption Force

We assume that the direction of net energy flux $\hat{\mathbf{S}}$ lies at angle θ_{rad} with respect to the grain’s spin axis $\hat{\boldsymbol{\omega}}^3$. We adopt a coordinate system with the z-axis lying along $\hat{\boldsymbol{\omega}}$ and the x-axis oriented so that $\hat{\mathbf{S}}$ lies in the x-z plane. The z-axis serves as the polar axis for spherical coordinates, with the x-axis the reference for azimuth; thus the spherical coordinates for $\hat{\mathbf{S}}$ are $(\theta_{\text{rad}}, 0)$. The “radiation” angle θ' is given by

$$\cos \theta' = \sin \theta_{\text{rad}} \sin \theta \cos \phi + \cos \theta_{\text{rad}} \cos \theta \quad . \quad (19)$$

We assume that both the photodesorbed H atoms and newly-formed H₂ molecules emerge symmetrically with respect to the local surface normal, with a “cosine-law” angular distribution, as adopted for photoelectrons. The momenta of the outgoing atoms and molecules are denoted by p_H and p_{H_2} respectively. We ignore polarization of the outgoing atoms and molecules when the grain has non-zero charge. The momentum transfer, per surface site, due to each of the contributing processes is directed radially inwards, with rates as summarized in Table 1. The factors of 2/3 appearing in Table 1 are due to the cosine-law angular distribution. For reflections and sticking, the term in brackets is the probability that the process will occur; we include the absorption of the gas-phase momentum of an arriving atom which will immediately undergo H₂ formation in the “sticking” category. The probability that the component of a gas H atom’s velocity along the surface normal lies between v and $v + dv$ is given by $P(v)dv = (\beta/\pi)^{1/2} \exp(-\beta v^2)dv$.

Integrating the momentum transfer rates over all surface sites yields the photodesorption force:

$$\frac{\mathbf{F}_{\text{pd}}}{\gamma \pi a^2} = -\hat{\mathbf{z}} \int_0^\pi d\theta \sin \theta \cos \theta f(\theta) [C + \bar{\Psi}(\theta)] - \hat{\mathbf{x}} \int_0^\pi d\theta \sin^2 \theta f(\theta) \frac{1}{2\pi} \int_0^{2\pi} d\phi \cos \phi \Psi(\theta') \quad , \quad (20)$$

where

$$\gamma \equiv \frac{4R_{\text{pd}}^0 p_H}{3l^2} \quad (21)$$

³We consider θ_{rad} to be constant; i.e. we ignore the likely precession of $\hat{\boldsymbol{\omega}}$ about the magnetic field.

and

$$C \equiv \frac{1}{\alpha} \left[s_c \left(\frac{2E_{\text{H}_2}}{E_{\text{H}}} \right)^{1/2} + \frac{3}{4} \left(\frac{\pi kT}{E_{\text{H}}} \right)^{1/2} (s_{\text{H}} - s_c) \right] . \quad (22)$$

Since the H arrival rate does not depend on surface location for a non-drifting grain, the contributions due to H₂ formation, reflections, and sticking depend only on $f(\theta)$ and are thus directed along $\hat{\mathbf{z}} = \hat{\boldsymbol{\omega}}$; they are all accounted for in the constant C . For rapidly flipping grains, $f(\theta) = f(\pi - \theta)$, so that only photodesorption contributes to the momentum transfer; this is also true for non-flipping grains when $\theta_{\text{rad}} = 90^\circ$. In these cases, for given $\{\gamma, s_{\text{H}}, s_c, \text{radiation field}\}$, the maximum force occurs when $n_{\text{H}} \rightarrow \infty$, so that $\alpha \rightarrow 0$, $f(\theta) \rightarrow \text{constant}$, and

$$\mathbf{F}_{\text{pd}} \rightarrow \mathbf{F}_{\text{pd}}^{\text{m}} \equiv -\gamma\pi a^2 \frac{s_{\text{H}}}{s_{\text{H}} + s_c} \hat{\mathbf{S}} \int_0^\pi d\theta' \sin\theta' \cos\theta' \Psi(\theta') . \quad (23)$$

When $f(\theta) \neq f(\pi - \theta)$, the magnitude of \mathbf{F}_{pd} can be much greater than F_{pd}^{m} , depending on the value of C . For example, when $\alpha \ll 1$ and $\alpha C \gg 1$, $F_{\text{pd}} \approx \alpha C F_{\text{pd}}^{\text{m}} / (s_{\text{H}} + s_c)$, for non-flipping grains. However, for realistic parameter choices and interstellar conditions, it is usually the case that $F_{\text{pd}} \leq F_{\text{pd}}^{\text{m}}$. Also note that, for non-flipping grains with $\theta_{\text{rad}} = 0$, $F_{\text{pd}} = 0$ when $\alpha C = s_{\text{H}} + s_c$. In this case, the contributions from the various momentum transfer processes exactly balance, regardless of the functional form of $\Psi(\theta')$; of course, such a parameter conspiracy is unlikely for real grains in the ISM.

4.5. Computational Results

In Figure 9 (lower panel), we display the photodesorption asymmetry integral that appears in equation (23) for F_{pd}^{m} , for carbonaceous and silicate grains. This integral takes nearly the same values for the ISRF as for a blackbody (cut off at 13.6 eV) with $T_c = 3 \times 10^4$ K. We found in Figures 2 and 3 that, for some grain sizes and photon energies, the electric intensity just below the grain surface is unexpectedly concentrated in the hemisphere facing away from the radiation. The same effect occurs with the external electric intensity, and leads to a “backwards” photodesorption force, for a range of grain sizes.

In the top panel of Figure 9, we plot $F_{\text{pd}}^{\text{m}}/F_{\text{rad}}$ for our canonical parameter values, given in Table 2. The surface site area of $l^2 = 6 \text{ \AA}^2$ would result if a site is a hexagon in a graphite sheet with C–C spacings of $\approx 1.5 \text{ \AA}$. We assume that photodesorbed H atoms carry kinetic energy $E_{\text{H}} = 2 \text{ eV}$ and newly-formed molecules carry kinetic energy $E_{\text{H}_2} = 1 \text{ eV}$, implying $p_{\text{H}} = p_{\text{H}_2}$ (note that p_{H_2} is not relevant for the calculation of F_{pd}^{m} , though). For large grains the photodesorption force dominates the radiation pressure for the blackbody spectrum, but is not nearly so important for the ISRF.

In the upper panel of Figure 10 we display $F_{\text{pd}}/F_{\text{pd}}^{\text{m}}$ for non-flipping carbonaceous grains with

$a = 0.3\mu\text{m}$, for a few values of α .⁴ We also assume that $s_{\text{H}} = s_{\text{c}} = 1$, $p_{\text{H}_2} = p_{\text{H}}$, and a blackbody radiation spectrum (cut off at 13.6 eV) with $T_{\text{c}} = 3 \times 10^4 \text{K}$. In the lower panel of Figure 10 we display $\cos \theta_{\text{f}}$, where θ_{f} is the angle between \mathbf{F}_{pd} and $\hat{\mathbf{S}}$. The results for other grain sizes for which F_{pd} is significant, for silicates, and for illumination by the ISRF are very similar.

As θ_{rad} increases, H atoms which stick to sites on the “dark” side of the grain have greater opportunity to photodesorb from the side facing the radiation, as they are transported there by the rotation; thus the photodesorption force increases with θ_{rad} . For flipping grains, the occupation fraction f depends only mildly on θ (Figure 11), so that $F_{\text{pd}} \approx F_{\text{pd}}^{\text{m}}$ and $\cos \theta_{\text{f}} \approx 1$ for all values of θ_{rad} .

In Figure 12 we plot $F_{\text{pd}}/F_{\text{pd}}^{\text{m}}$ and $\cos \theta_{\text{f}}$ for $s_{\text{c}} = 0.1$ and various combinations of α and $(kT/E_{\text{H}})^{1/2}$; otherwise the parameters are the same as for Figure 10. When $\alpha = (kT/E_{\text{H}})^{1/2} = 0.01$, $\cos \theta_{\text{f}}$ is very nearly 1 for all values of θ_{rad} , much more so than when $s_{\text{c}} = 1$ and $\alpha = 0.01$. Although $f(\theta)$ is somewhat more constant for the case with $s_{\text{H}} = 1$, C is also substantially larger, and it accounts for the bulk of the component perpendicular to $\hat{\mathbf{S}}$. When $(kT/E_{\text{H}})^{1/2} = 1$, C is large enough that $\cos \theta_{\text{f}} \approx -1$ for $\theta_{\text{rad}} = 0$.

5. Drag Forces

Baines et al. (1965) calculated the drag force on a spherical particle drifting through a dilute gas, assuming that colliding atoms reflect elastically. Draine & Salpeter (1979) obtained an analytical expression which accurately reproduces the Baines et al. numerical results, and this is widely employed in studies of drifting interstellar grains. For subsonic drift speeds, the drag due to collisions with neutral atoms of element j , in the absence of surface processes, is given by

$$F_{\text{drag},j}^0 \approx \pi a^2 \frac{8}{3} n_j v_{\text{d}} \left(\frac{2m_p kT}{\pi} \right)^{1/2} A_j^{1/2}, \quad (24)$$

where n_j and A_j are the number density and mass number of element j , respectively.

The Coulomb drag, due to interactions with distant ions, is often important in interstellar applications. For subsonic drift speeds, the Coulomb drag is given by

$$F_{\text{drag,Coul}} \approx F_{\text{drag,H}}^0 \times \frac{1}{2} \sum_i x_i \left(\frac{m_i}{m_p} \right)^{1/2} \sum_Z f_Z \left(\frac{Ze^2}{akT} \right)^2 \ln \left[\frac{3(kT)^{3/2}}{2e^3 |Z| (\pi x n_{\text{H}})^{1/2}} \right] \quad (25)$$

(Draine & Salpeter 1979). The sum is over ions i , and $x = \sum_i x_i$. Since the grain charge fluctuates on a time scale short compared to the drag time, we average over charge states. The dominant ions in neutral gas are C^+ and H^+ . We take the gas-phase C abundance to be $\text{C}/\text{H} = 1.4 \times 10^{-4}$

⁴For our assumed carbonaceous grain parameter values, $G/n_{\text{H}} \approx 4.4 \times 10^{-3} \alpha \sqrt{T} \text{K}^{-1/2} \text{cm}^3$.

(Cardelli et al. 1996; Sofia et al. 1997). Thus, when calculating $F_{\text{drag,Coul}}$, we assume that $x_{\text{C}} = x$, $x_{\text{H}} \approx 0$ when $x \leq 1.4 \times 10^{-4}$, and $x_{\text{C}} = 1.4 \times 10^{-4}$, $x_{\text{H}} = x - 1.4 \times 10^{-4}$ when $x > 1.4 \times 10^{-4}$.

Next, we consider how the surface processes considered in the previous section, namely H_2 formation and photodesorption, affect the drag force $\mathbf{F}_{\text{drag,H}}$ due to collisions with atomic H.

For a drifting grain, the arrival rate R_{arr} depends on the angle θ'' with respect to the grain's velocity \mathbf{u} :

$$R_{\text{arr}}(\theta'') = R_{\text{arr}}^0 D(\theta'') \quad , \quad (26)$$

where

$$D(\theta'') = \exp(-y^2) + \sqrt{\pi}y \left[1 + \frac{2}{\sqrt{\pi}} \int_0^y dt \exp(-t^2) \right] \quad , \quad (27)$$

with $y \equiv \sqrt{\beta}u \cos \theta''$. The expansion

$$D(\theta'') \approx 1 + \sqrt{\pi}y + y^2 - \frac{1}{6}y^4 \quad (28)$$

is accurate to within 1% for $-0.653 \leq y \leq 1.05$.

The momentum transfer rates due to reflections and sticking are modified from the non-drifting case by $P(v)v^2 \rightarrow P(v)(v + u \cos \theta'')^2$ in Table 1 (and the lower integrand is now $-u \cos \theta''$). The rates obtained for non-drifting grains must be multiplied by the factor $2E(\theta'')/\sqrt{\pi}$, where

$$\begin{aligned} E(\theta'') &= y \exp(-y^2) + (1 + 2y^2) \left(\frac{\sqrt{\pi}}{2} + \int_0^y \exp(-t^2) dt \right) \\ &\approx \frac{\sqrt{\pi}}{2} + 2y + \sqrt{\pi}y^2 + \frac{2}{3}y^3 - \frac{1}{15}y^5 \quad . \end{aligned} \quad (29)$$

The expansion in equation (29) is accurate to within 1% for $-0.749 \leq y \leq 1.43$.

Photodesorption substantially complicates the drag, since the occupation fraction is no longer constant, but is given by

$$f(\theta) = s_{\text{H}} \left[s_{\text{H}} + s_{\text{c}} + \alpha \frac{\bar{\Psi}(\theta)}{\bar{D}(\theta)} \right]^{-1} \quad , \quad (30)$$

for non-flipping grains. Of course, for flipping grains $\bar{\Psi}(\theta)/\bar{D}(\theta)$ is replaced by $[\bar{\Psi}(\theta) + \bar{\Psi}(\pi - \theta)]/[\bar{D}(\theta) + \bar{D}(\pi - \theta)]$ in equation (30). The drag force can be found by evaluating the total force resulting from collisions of H with the grain (i.e. $\mathbf{F}_{\text{pd}} + \mathbf{F}_{\text{drag,H}}$) and subtracting \mathbf{F}_{pd} ; the total force is given by

$$\begin{aligned} \mathbf{F}_{\text{pd}} + \mathbf{F}_{\text{drag,H}} &= -\frac{a^2}{l^2} \int_0^\pi d\theta \sin \theta \int_0^{2\pi} d\phi \\ &\left\{ \frac{2}{3} R_{\text{pd}}^0 p_{\text{H}} f(\theta) \Psi(\theta') + \frac{2}{3} R_{\text{arr}}^0 s_{\text{c}} p_{\text{H}_2} f(\theta) D(\theta'') + [2 - s_{\text{H}} + f(\theta)(s_{\text{H}} - s_{\text{c}})] \frac{m_{\text{p}}}{\sqrt{\beta}} R_{\text{arr}}^0 E(\theta'') \right\} \\ &[\hat{\mathbf{z}} \cos \theta + \hat{\mathbf{x}} \sin \theta \cos \phi + \hat{\mathbf{y}} \sin \theta \sin \phi] \quad . \end{aligned} \quad (31)$$

To first order in u , equation (31) yields, for flipping grains,

$$\frac{\mathbf{F}_{\text{drag,H}}}{F_{\text{drag,H}}^0} = -\frac{2 - s_{\text{H}}}{2} \hat{\mathbf{u}} - \frac{3}{8} \left[s_{\text{H}} - s_{\text{c}} + \frac{s_{\text{c}} p_{\text{H}_2}}{3} \left(\frac{\pi}{2m_p kT} \right)^{1/2} \right] \int_0^\pi d\theta \sin \theta f_0(\theta) [\sin^2 \theta \hat{\mathbf{u}} - (1 - 3 \cos^2 \theta) \cos \theta_{\text{u}} \hat{\boldsymbol{\omega}}] \quad , \quad (32)$$

where $f_0(\theta)$ is the occupation fraction that would hold for the same grain if $u = 0$. For non-flipping grains, the following term must be added to the right-hand side of equation (32):

$$-\frac{\alpha \cos \theta_{\text{u}}}{4s_{\text{H}}} \int_0^\pi d\theta \sin \theta \cos \theta f_0^2(\theta) \bar{\Psi}(\theta) [\mathbf{J}_1(\theta) + \mathbf{J}_2(\theta)] \quad , \quad (33)$$

where

$$\mathbf{J}_1(\theta) = \hat{\mathbf{z}} \cos \theta \left[\frac{3\pi}{4} (s_{\text{H}} - s_{\text{c}}) + s_{\text{c}} p_{\text{H}_2} \left(\frac{\pi}{2m_p kT} \right)^{1/2} \right] \quad (34)$$

and

$$\mathbf{J}_2(\theta) = \alpha p_{\text{H}} \left(\frac{\pi}{2m_p kT} \right)^{1/2} \left[\hat{\mathbf{z}} \cos \theta \bar{\Psi}(\theta) + \hat{\mathbf{x}} \sin \theta \frac{1}{2\pi} \int_0^\pi d\phi \cos \phi \Psi(\theta') \right] \quad . \quad (35)$$

The above approximation works best for small a and α . For the range of conditions $T \in (50, 6000)$ K and $\sqrt{\beta}u \leq 0.1$, it is valid to within 1% when $a \leq 0.1 \mu\text{m}$, $\alpha \leq 1$; 3% when $a \leq 1 \mu\text{m}$, $\alpha \leq 1$; 10% when $a \leq 0.1 \mu\text{m}$, $\alpha \leq 10$; and 30% when $a \leq 1 \mu\text{m}$, $\alpha \leq 10$. The direction of $\mathbf{F}_{\text{drag,H}}$ can differ substantially from $-\mathbf{u}$ when $\alpha \geq 1$, depending on the relative orientations of \mathbf{u} , $\hat{\boldsymbol{\omega}}$, and $\hat{\mathbf{S}}$.

6. Starlight Anisotropy

Here we estimate the radiation field anisotropy in the diffuse ISM, by considering the solar neighborhood to be typical and adding up the flux density over the entire sky. Most of the flux in the visible and UV comes directly from stars; starlight scattered off of dust grains (the diffuse galactic light, DGL) makes a non-negligible additional contribution (see, e.g., Witt 1989). Ideally, we would like to have a catalog of stars with accurate photometry and complete down to the magnitude beyond which fainter stars do not significantly contribute, along with accurate photometry of the DGL.

Although this ideal is not currently available, there are a few catalogs from which useful estimates can be made. The Skymap Star Catalog, Version 3.7 (Slater & Hashmall 1992) is claimed to be complete down to magnitude 9 in the B and V bands, and the Tycho Catalog (ESA 1997) is claimed to be 99.9% complete down to $V \sim 10.5$. However, the photometry is missing for thousands of stars in the Tycho Catalog, including many bright stars. In Figure 13 we plot the integrated energy densities per unit frequency u_ν , normalized to the ISRF, as a function of the limiting stellar magnitude. The Skymap results are for the Johnson B and V bands (B_{J} and V_{J} respectively); the Tycho bands B_{T} and V_{T} closely resemble the corresponding Johnson bands. The Tycho catalog also gives indirectly-derived values for V_{J} for all stars, including those for which Tycho photometry

is missing. The B_T and V_T energy densities are systematically lower than the B_J and V_J energy densities due to omission of stars lacking Tycho photometry. The V_J fluxes from the two catalogs agree very well, except at the limit of the Skymap catalog. Note that at magnitude 10 the curves are still concave up, with the integrated starlight accounting for less than half of the ISRF.

The normalized starlight dipole moment is given by

$$\mathbf{p}_s = \frac{\sum_s u_\nu(s) \hat{\mathbf{n}}(s)}{u_\nu(\text{ISRF})}, \quad (36)$$

where $u_\nu(s)$ is the energy density per frequency interval due to star s and $\hat{\mathbf{n}}(s)$ is the direction to star s . In Figure 14 we plot p_s . Again, the B_T and V_T results are offset, because of the absence of photometry for bright stars. The abrupt decrease in the V band normalized dipole moment at the faint end of the Skymap catalog is probably incorrect. It is unlikely that the fainter stars and DGL would conspire to produce an anisotropy directed opposite to that resulting from the brighter stars; thus it appears that the anisotropy in B (V) is at least 5% (3%). For B , the (right ascension, declination) of the anisotropy remain quite constant for limiting magnitudes of 4 through 9, with value $(115^\circ, -43^\circ)$. For V , the anisotropy direction gradually shifts to $(115^\circ, -51^\circ)$ at magnitude 10.5.

The best available catalog for studying the anisotropy in the UV was constructed by the S2/68 experiment (Boksenberg et al. 1973) on the European Space Research Organization’s TD-1 satellite, which provided broadband flux measurements in four channels. The full catalog was not published, but Gondhalekar, Phillips, & Wilson (1980) presented tables of the integrated starlight in hundreds of patches, covering the entire sky. Gondhalekar et al. also estimated the flux contribution from the DGL and from stars too faint to be included in the catalog, using background data. In some cases, two or more stars were observed simultaneously. Such blended stars were excluded from the catalog, and Gondhalekar et al. estimated their contribution to the total flux, although the distribution of these unresolved stars on the sky was not reported. The Mathis et al. (1983) ISRF was constructed to maximize consistency with the Gondhalekar et al. (1980) results and with other, limited-coverage UV surveys. The adopted ISRF fluxes are somewhat higher than the total fluxes of Gondhalekar et al.

In estimating the dipole in the UV, we use tables of integrated starlight in $10^\circ \times 10^\circ$ patches in Gondhalekar (1989). These differ somewhat from the fluxes in Gondhalekar et al. (1980), because the absolute calibration of the S2/68 experiment was revised. In Table 3 we give νu_ν and the normalized dipole moment p_s for the four UV bands; the listed dipole moments are likely lower limits. Note that the normalized dipole moment is substantially greater in the UV than in the visible. This difference presumably results from the differences in the stellar populations giving rise to the two spectral regions and the greater importance of extinction by dust in the UV. The UV radiation is dominated by early-type stars, which are relatively few in number and hence less evenly distributed than main sequence stars in general, all of which contribute to the visible radiation. In Table 4 we display the direction of the anisotropy for all of the considered bands.

For simplicity, we will assume that the anisotropy is independent of wavelength when calculating drift speeds in the following section. We will adopt an anisotropy of 10%, intermediate between the anisotropies inferred for the visible and the UV.

7. Gas-Grain Drift in the Diffuse ISM

We will estimate drift speeds for grains in the cold neutral medium (CNM; $T = 100\text{ K}$, $n_{\text{H}} = 30\text{ cm}^{-3}$, $n_e = 0.045\text{ cm}^{-3}$) and the warm neutral medium (WNM; $T = 6000\text{ K}$, $n_{\text{H}} = 0.3\text{ cm}^{-3}$, $n_e = 0.03\text{ cm}^{-3}$).

In the presence of a magnetic field \mathbf{B} , the steady state drift velocity is given by

$$(v_{\parallel}, v_{\perp}, v_{\perp\perp}) = \frac{F}{\kappa} \left(\cos\theta, \frac{\sin\theta}{1 + (\omega\tau)^2}, \frac{\omega\tau \sin\theta}{1 + (\omega\tau)^2} \right) \quad (37)$$

where \mathbf{F} is the net force excluding the magnetic and drag forces, $\mathbf{F}_{\text{drag}} = -\kappa\mathbf{v}_d$, θ is the angle between \mathbf{B} and \mathbf{F} , $\omega\tau = ZeB/c\kappa$ is the product of the gyrofrequency and gas-drag time, and the subscripts (\parallel , \perp , $\perp\perp$) denote components (parallel to \mathbf{B} , perpendicular to \mathbf{B} and in the plane spanned by \mathbf{B} and \mathbf{F} , perpendicular to the plane spanned by \mathbf{B} and \mathbf{F}). Thus, drift across magnetic field lines is suppressed by a factor $[1 + (\omega\tau)^2]^{1/2}$.

We display F_{pe} and F_{pd} for the CNM and WNM in Figure 15, and $F_{\text{drag,H}}$ and $F_{\text{drag,Coul}}$ in Figure 16. In order to estimate the largest effect that photodesorption is likely to have, we adopt $\theta_{\text{rad}} = 90^\circ$ (i.e. spin axis perpendicular to the net radiation flux); in this case $\mathbf{F}_{\text{pd}} \parallel \hat{\mathbf{S}}$ and $\mathbf{F}_{\text{drag,H}} \parallel -\hat{\mathbf{S}}$. In order to gauge the importance of the photoelectric and photodesorption forces, we compute drift speeds both with and without including them. Specifically, we consider the following three cases:

$$\text{Case I} \quad F_{\text{rad}} = F_{\text{drag,H}}^0 + F_{\text{drag,He}} + F_{\text{drag,Coul}} \quad , \quad (38)$$

$$\text{Case II} \quad F_{\text{rad}} + F_{\text{pe}} = F_{\text{drag,H}}^0 + F_{\text{drag,He}} + F_{\text{drag,Coul}} \quad , \quad (39)$$

and

$$\text{Case III} \quad F_{\text{rad}} + F_{\text{pe}} + F_{\text{pd}} = F_{\text{drag,H}} + F_{\text{drag,He}} + F_{\text{drag,Coul}} \quad . \quad (40)$$

The resulting drift speeds are plotted in Figures 17 and 18. For $a > 0.1\mu\text{m}$ carbonaceous grains, we find drift speeds $v_d > 0.01\text{ km s}^{-1}$ in the CNM, and $v_d > 0.15\text{ km s}^{-1}$ in the WNM; for $a > 0.1\mu\text{m}$ silicate grains, we find $v_d > 0.002\text{ km s}^{-1}$ in the CNM, and $v_d > 0.1\text{ km s}^{-1}$ in the WNM. The softness of the ISRF prevents F_{pe} and F_{pd} from substantially increasing the drift speeds over those that would hold if only F_{rad} were acting. These drift speeds were determined under the assumption that the radiation flux $\hat{\mathbf{S}}$ is along the magnetic field. As seen in Figure 19, the suppression factor for drift perpendicular to the field is substantial even for micron-sized grains.

7.1. Consequences

Since grains of different sizes drift with different speeds, grains collide, with coagulation likely at low collision speeds. As $a \rightarrow 0$, $v_d \rightarrow 0$, so that if grains always stick upon colliding, the timescale t_a for a very small grain to become attached to another grain is given by

$$t_a^{-1} \approx \pi \int_{a_{\min}}^{a_{\max}} a^2 v_d(a) \frac{dn_{\text{gr}}}{da} da. \quad (41)$$

Here we estimate the maximum likely values for t_a in the CNM and WNM, by adopting the drift speeds computed for case III above (i.e., including surface processes and assuming $\hat{\mathbf{S}} \parallel \mathbf{B}$; t_a is only slightly longer for cases I or II). We adopt the grain size distribution from Weingartner & Draine (2001a) with $R_V = 3.1$ and $b_C = 6 \times 10^{-5}$ (their favored distribution for the average diffuse ISM). For coagulation with the carbonaceous grain population, $t_a \approx 8 \times 10^9$ yr (6×10^{10} yr) in the CNM (WNM). For coagulation with the silicate population, $t_a \approx 1.5 \times 10^{10}$ yr (4×10^{10} yr) in the CNM (WNM). Thus, drift due to forces associated with anisotropic radiation apparently results in negligible coagulation in the diffuse ISM.

Gas-grain drift can also lead to variations in the dust-to-gas ratio. If the size of a cold neutral medium region is ~ 1 pc, then the time to separate micron-sized grains from the region could be as short as $\approx 2 \times 10^7$ yr, which is perhaps comparable to the cloud lifetime.

8. Summary

We have investigated two forces that act on dust grains exposed to anisotropic radiation fields, due to the asymmetric photon-stimulated emission of particles from the grains. First, we have improved on Lafon’s (1990) treatment of the photoelectric force, due to the recoil associated with photoelectrons, by using the realistic prescription of Kerker & Wang (1982) for estimating the emission asymmetry and employing the recent photoemission model of Weingartner & Draine (2001b).

The photoelectric force depends on the ambient conditions relevant to the grain charging, including the shape of the radiation spectrum and the parameter $G\sqrt{T}/n_e$. We find that the photoelectric force is comparable to the radiation pressure in regions where the grain potential is relatively low and the radiation spectrum is relatively hard (Figures 4–6). We find that the photoelectric force is unimportant compared with the radiation pressure in the cold and warm neutral media for grains larger than a few hundred Å, because of the softness of the interstellar radiation field, as estimated by Mezger et al. (1982) and Mathis et al. (1983).

We have also investigated the force resulting from the asymmetric photodesorption of H atoms adsorbed on the grain surface. The surface physics and chemistry of likely grain materials are not currently well-known. We have adopted a very simple, yet plausible, model in order to examine the

potential importance of this force. In particular, we assume that H chemisorbs at all surface sites with sufficient binding energy to suppress thermal desorption and site-to-site diffusion.

In our model, the total force associated with gas-phase atoms which collide with the surface includes contributions from three processes: photodesorption, H₂ formation, and elastic reflection of atoms incident on the grain surface. We call the force on a grain that is not drifting with respect to the gas the “photodesorption” force. When the grain drifts, the total force (due to the above three processes) minus the photodesorption force equals the drag force, which is thus modified from the traditional treatment considering only the reflection of incident atoms (§5).

With our standard choices for parameter values (Table 2), we find that the photodesorption force dominates the radiation pressure for grains with $a \gtrsim 0.1\mu\text{m}$ when the radiation field is relatively hard (Figure 9). Laboratory studies of the surfaces of candidate grain materials, including determinations of photodesorption cross sections, are needed in order to clarify the true importance of this force.

Grains exposed to anisotropic radiation will drift relative to the gas due to the combined action of the radiation pressure, photoelectric force, and photodesorption force. We find that the radiation field in the diffuse ISM is $\sim 10\%$ anisotropic in the visible and ultraviolet (§6). In §7, we estimate the maximum likely drift speeds for grains in the cold and warm neutral media. We find the timescale for grain coagulation resulting from this drift to be $\gtrsim 5 \times 10^9$ yrs. Large grains ($a \sim 1\mu\text{m}$) might drift rapidly enough to be substantially separated from the gas in cold diffuse clouds. In a separate paper (Weingartner & Draine 2001c), we will investigate gas-grain drift in photodissociation regions.

This research was supported in part by NSF grant AST-9619429 and by NSF Graduate Research and International Fellowships to JCW. We are grateful to R. H. Lupton for the availability of the SM plotting package.

REFERENCES

- Baines, M. J., Williams, I. P., & Asebiomo, A. S. 1965, MNRAS, 130, 63
- Bakes, E. L. O., & Tielens, A. G. G. M. 1994, ApJ, 427, 822
- Bohren, C. F. & Huffman, D. R. 1983, Absorption and Scattering of Light by Small Particles (New York: Wiley)
- Cardelli, J. A., Meyer, D. M., Jura, M., & Savage, B. D. 1996, ApJ, 467, 334
- Draine, B. T. 1985, in Protostars and Planets II, ed. D. C. Black & M. S. Matthews (Tucson: Univ. Arizona Press), 621

- Draine, B. T. & Lee, H. M. 1984, *ApJ*, 285, 89
- Draine, B. T. & Salpeter, E. E. 1979, *ApJ*, 231, 77
- Draine, B. T., & Sutin, B. 1987, *ApJ*, 320, 803
- Draine, B. T., & Weingartner, J.C. 1996, *ApJ*, 470, 551
- Draine, B. T., & Weingartner, J.C. 1997, *ApJ*, 480, 633
- Franchy, R. 1998, *Rep. Prog. Phys.*, 61, 691
- Fromherz, T., Mendoza, C., & Ruetter, F. 1993, *MNRAS*, 263, 851
- Grevesse, N., Lambert, D. L., Sauval, A. J., van Dishoeck, E. F., Farmer, C. B., & Norton, R. H. 1991, *A&A*, 242, 488
- Habing, H. J. 1968, *Bull. Astron. Inst. Netherlands*, 19, 421
- Hall, J. S. 1949, *Science*, 109, 166
- Hall, J. S. & Mikesell, A. H. 1949, *AJ*54, 187
- Helling, B., Chakarov, D. V., Österlund, L., Zhdanov, V. P., & Kasemo, B. 1997, *J. Chem. Phys.*, 106, 982
- Hiltner, W. A. 1949a, *Science*, 109, 165
- Hiltner, W. A. 1949b, *ApJ*, 109, 471
- Hollenbach, D. J. & Salpeter, E. E. 1971, *ApJ*, 163, 155
- Kerker, M. & Wang, D.-S. 1982, *J. Coll. Interface Sci*, 85, 302
- Lafon, J.-P. J. 1990, *A&A*, 235, 490
- Laor, A. & Draine, B. T. 1993, *ApJ*, 402, 441
- Lazarian, A. & Draine, B. T. 1999a, *ApJ*, 516, L37
- Lazarian, A. & Draine, B. T. 1999b, *ApJ*, 520, L67
- Li, A., & Draine, B. T. 2001, *ApJ*, to be submitted
- Mathis, J. S., Mezger, P. G., & Panagia, N. 1983, *A&A*, 128, 212
- Mathis, J. S., Rumpl, W., & Nordsieck, K. H. 1977, *ApJ*, 217, 425
- Mendoza, C. & Ruetter, F. 1989, *Catal Lett*, 3, 89

- Mezger, P. G., Mathis, J. S., & Panagia, N. 1982, *A&A*, 105, 372
- Purcell, E. M. 1979, *ApJ*, 231, 404
- Roberge, W. G., Jones, D., Lepp, S., Dalgarno, A. 1991, *ApJS*, 77, 287
- Sofia, U. J., Cardelli, J. A., Guerin, K. P., & Meyer, D. M. 1997, *ApJ*, 482, L105
- Tielens, A. G. G. M. & Allamandola, L. J. 1987, in *Interstellar Processes*, eds. D. J. Hollenbach & H. A. Thronson, Jr. (Dordrecht: Reidel), 397
- van Dishoeck, E. F. 1987, *J. Chem. Phys.*, 86, 196
- van Dishoeck, E. F. & Dalgarno, A. 1984, *ApJ*, 277, 576
- Watson, W. D. 1972, *ApJ*, 176, 103
- Watson, W. D. 1973, *J. Opt. Soc. Am.*, 63, 164
- Weingartner, J. C. & Draine, B. T. 2001a, *ApJ*, in press [astro-ph/0008146]
- Weingartner, J. C. & Draine, B. T. 2001b, *ApJ*, submitted [astro-ph/9907251]
- Weingartner, J. C. & Draine, B. T. 2001c, in preparation

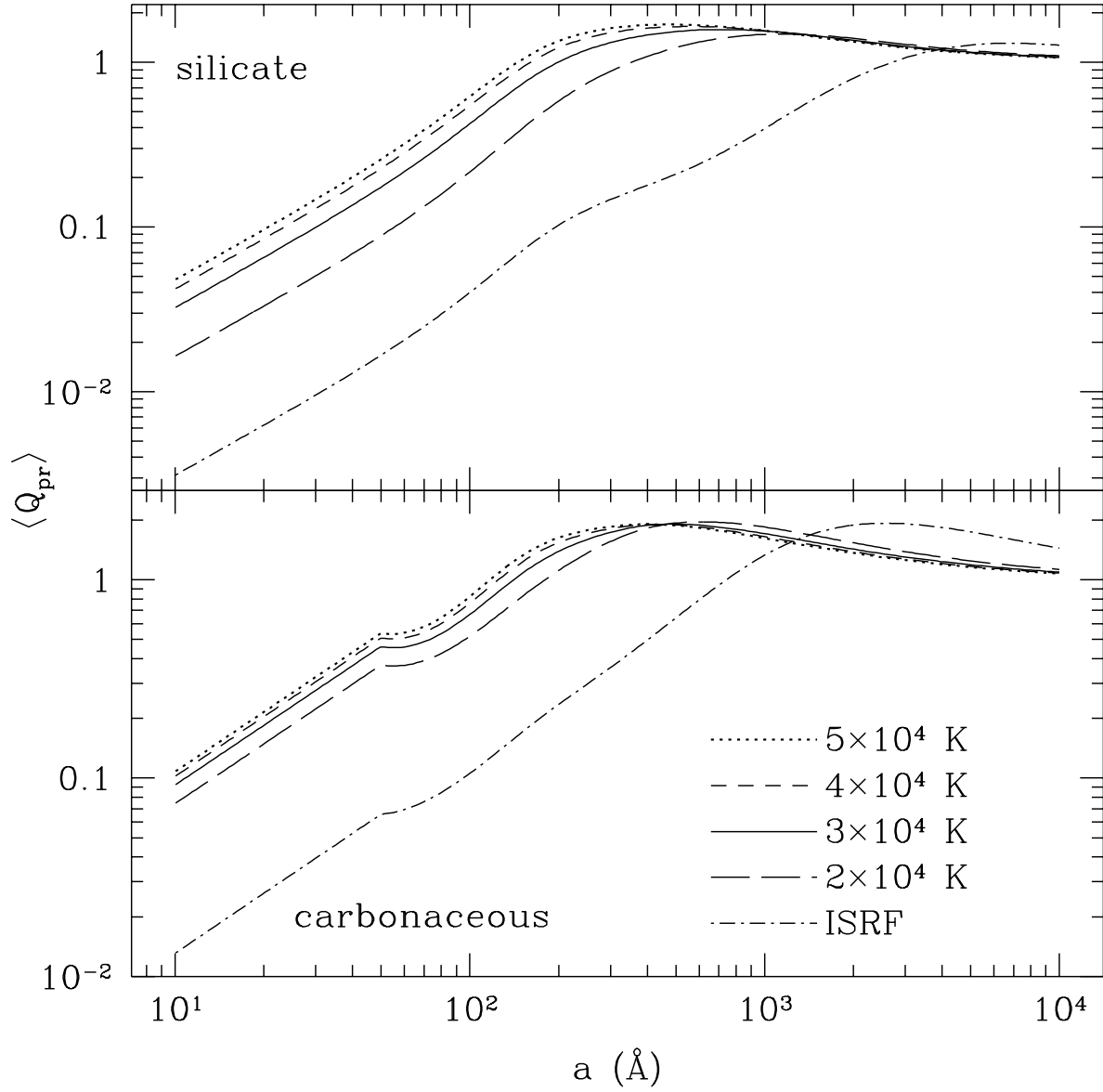


Fig. 1.— Radiation pressure efficiency factors for neutral carbonaceous and silicate grains, averaged over the interstellar radiation field (ISRF) and blackbody spectra with indicated color temperatures (cut off at 13.6 eV). The kink at $a = 50 \text{ \AA}$ results from the Li & Draine (2001) prescription for blending PAH and graphite optical properties.

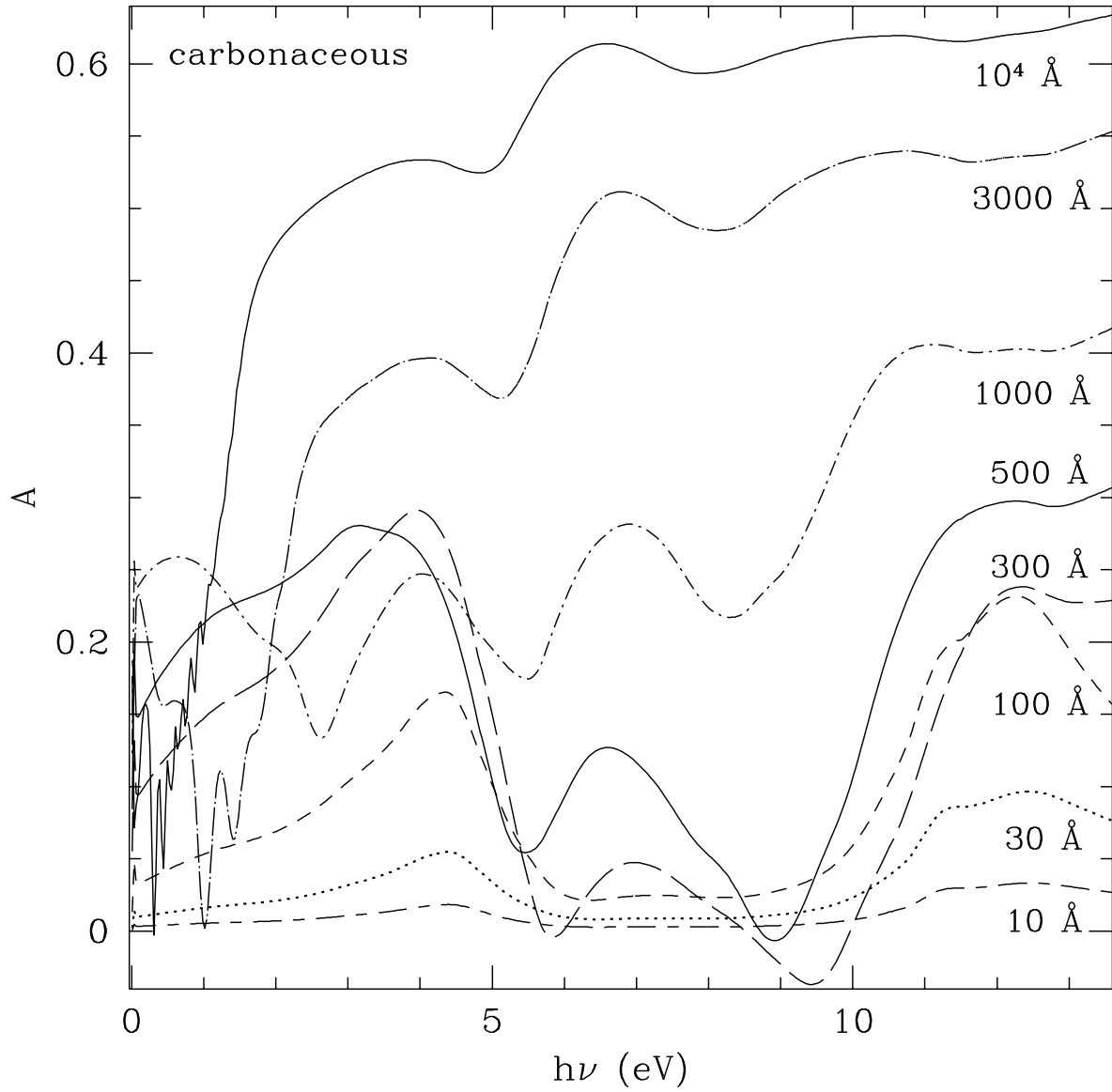


Fig. 2.— The asymmetry factor A as a function of the incident photon energy $h\nu$, for carbonaceous grains. The grain radius is indicated for each curve.

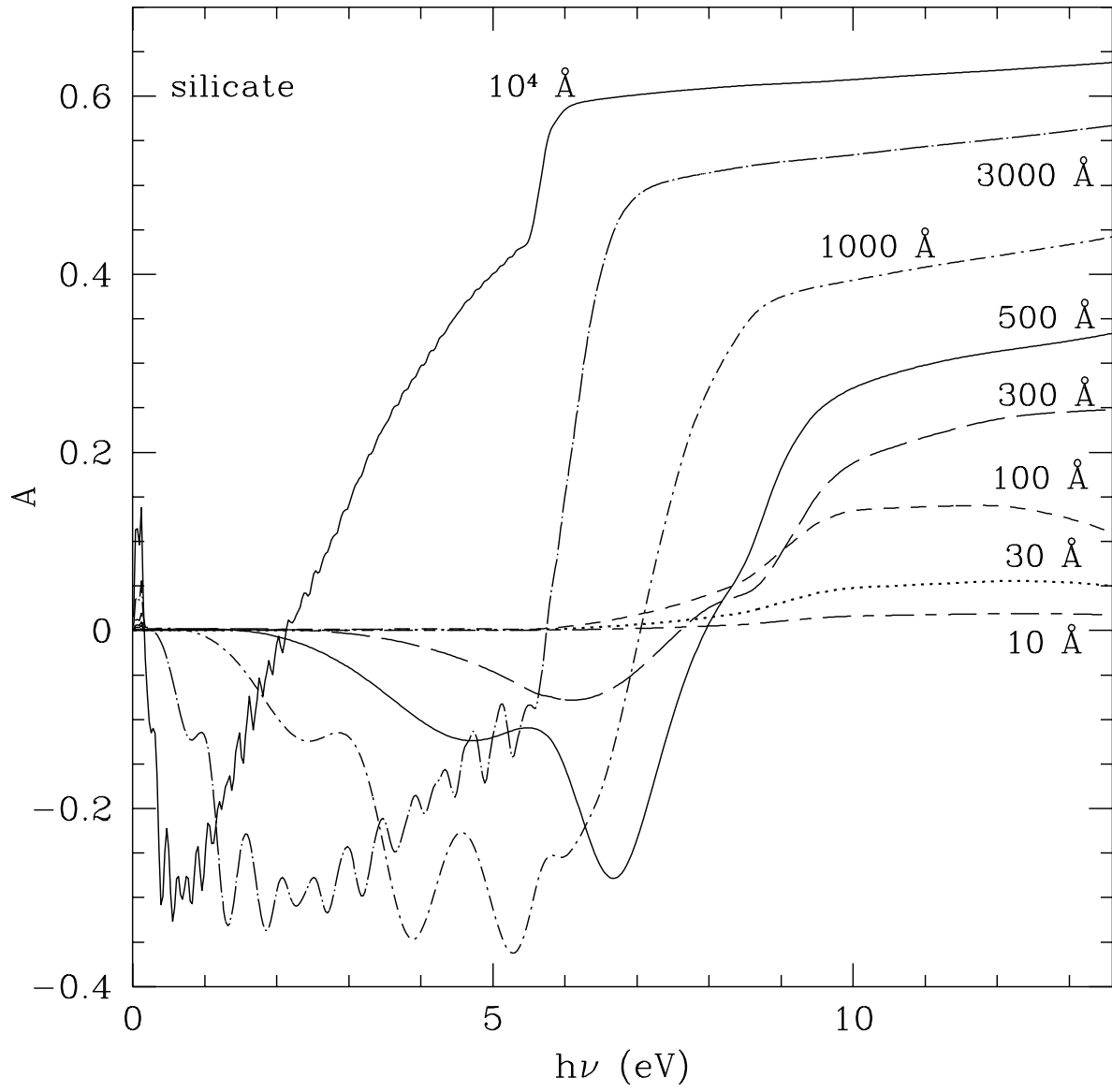


Fig. 3.— Same as Figure 2, but for silicate grains.

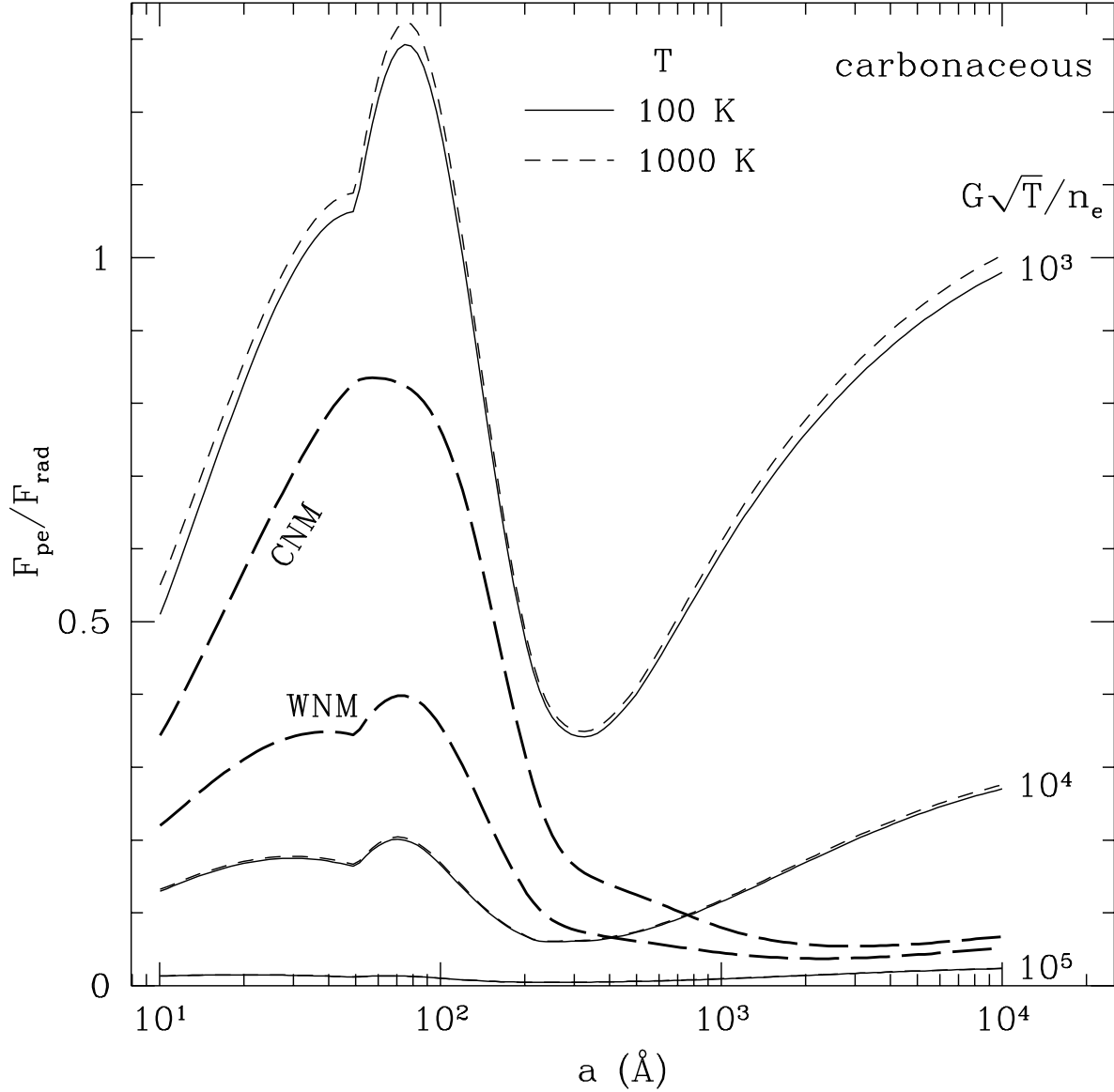


Fig. 4.— $F_{\text{pe}}/F_{\text{rad}}$ for carbonaceous grains, $T_c = 3 \times 10^4$ K, and two gas temperatures: 100 K (solid) and 1000 K (dashed). The values of $G\sqrt{T}/n_e$, in $\text{K}^{1/2} \text{cm}^3$, are indicated. Curves labelled CNM (WNM) are for cold (warm) neutral media and the ISRF.

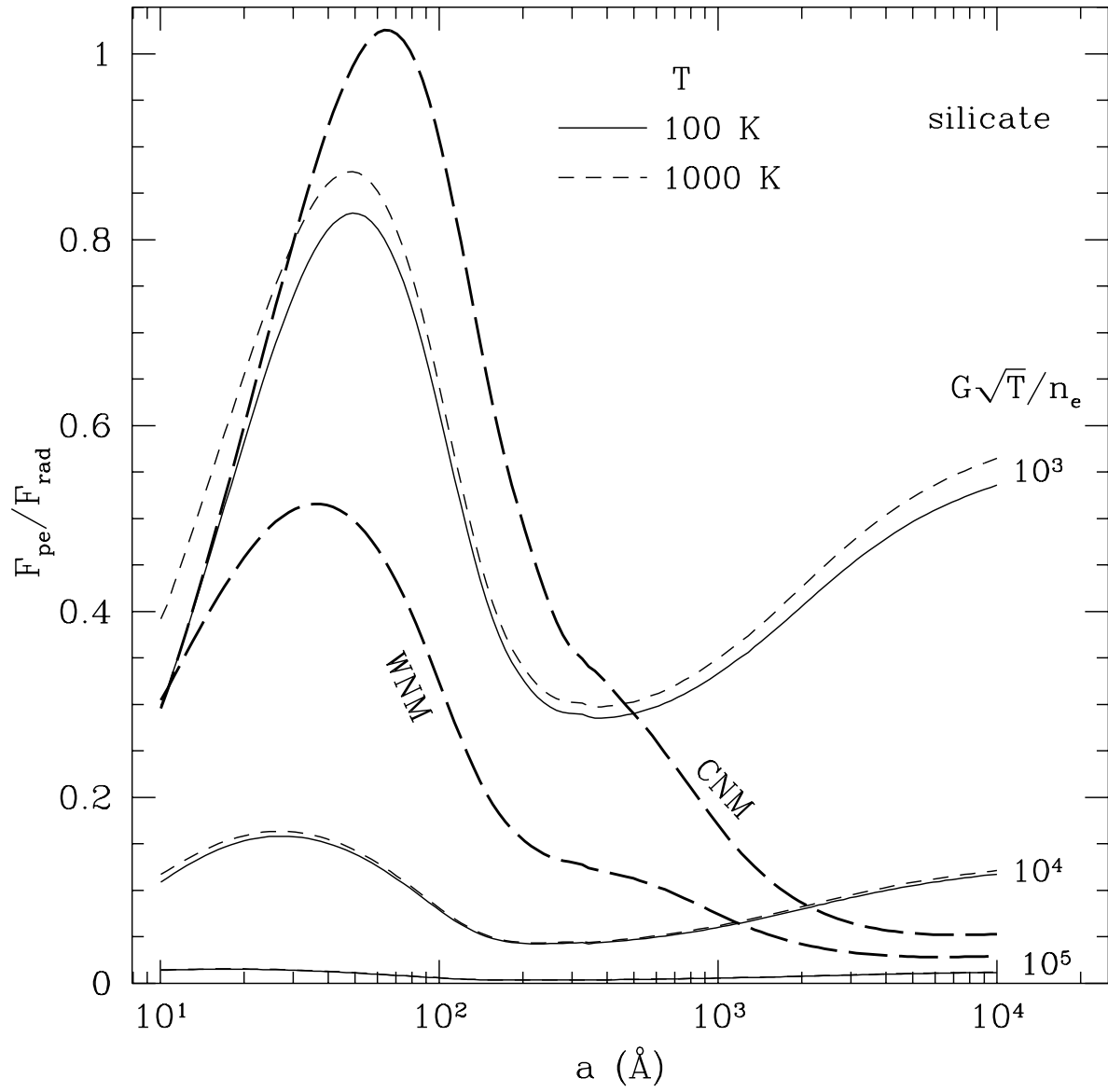


Fig. 5.— Same as Figure 4, but for silicate grains.

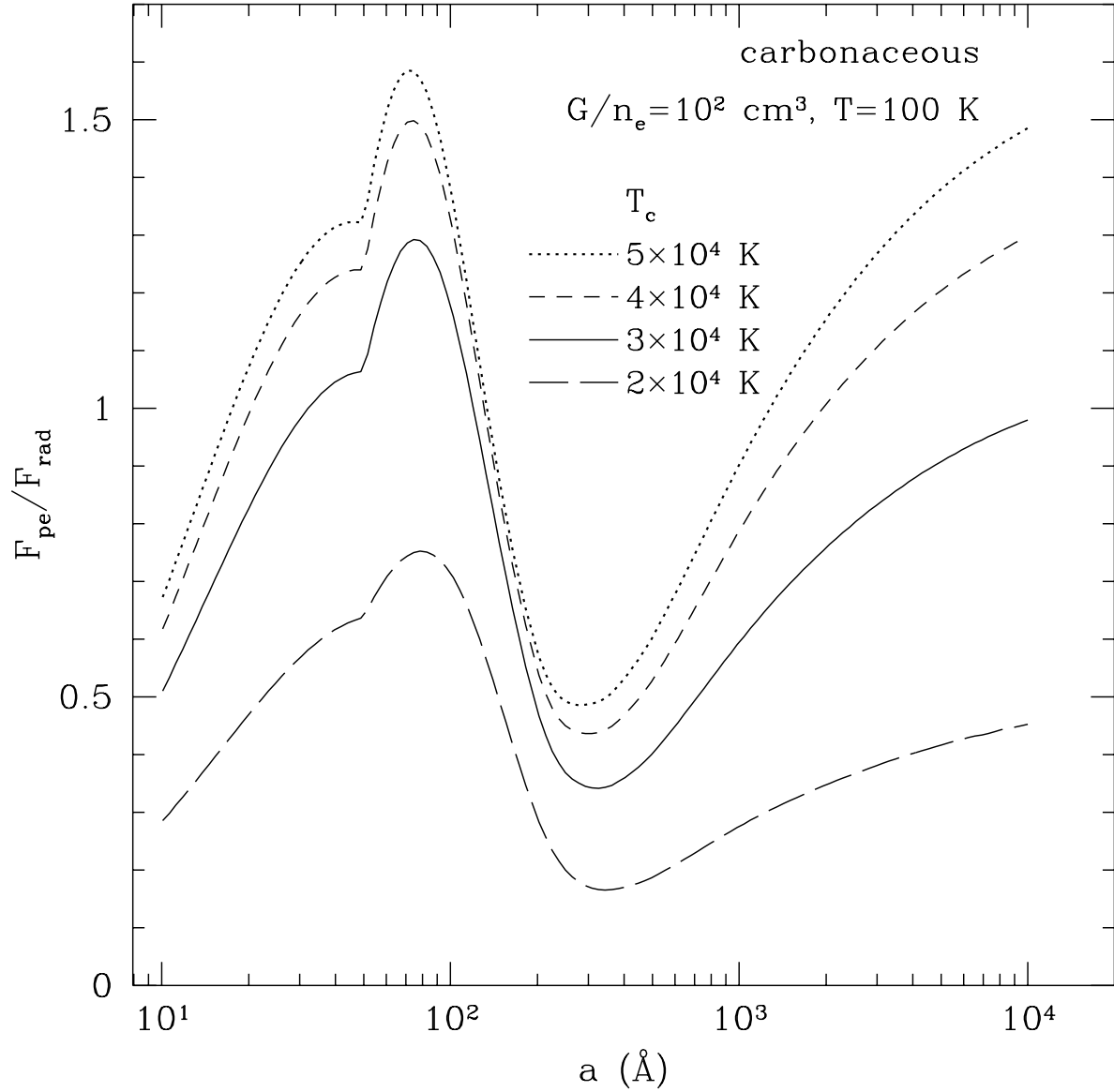


Fig. 6.— F_{pe}/F_{rad} for carbonaceous grains, $T = 100 \text{ K}$, $G\sqrt{T}/n_e = 10^3 \text{ K}^{1/2} \text{ cm}^3$, and four values of T_c as indicated. In all cases, the radiation field is assumed to be cut off at 13.6 eV .

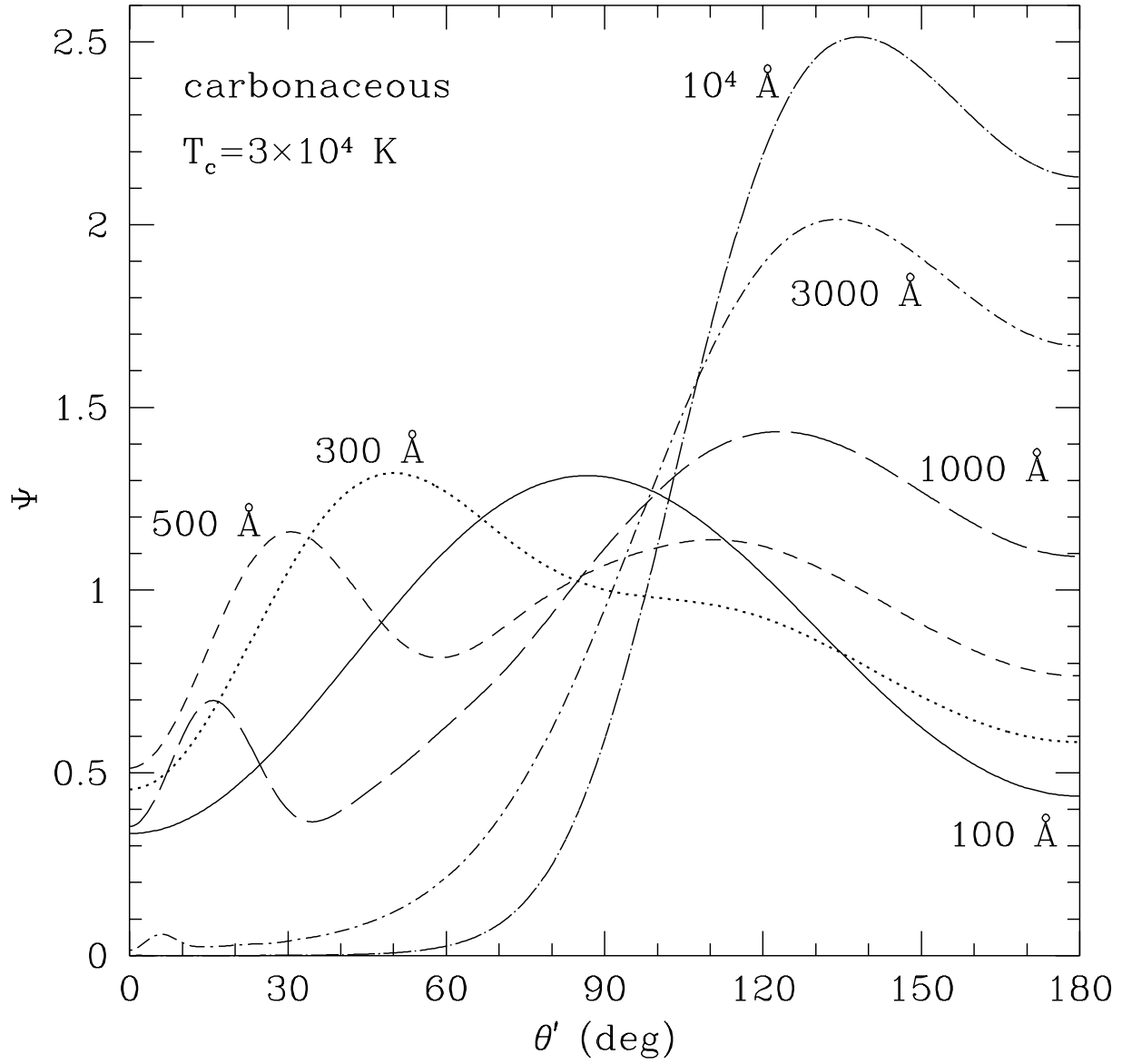


Fig. 7.— Normalized rate for photodesorption $\Psi(\theta')$ for carbonaceous grains, a blackbody radiation spectrum (cut off at 13.6 eV) with $T_c = 3 \times 10^4$ K, and several values of grain size a , as labeled.

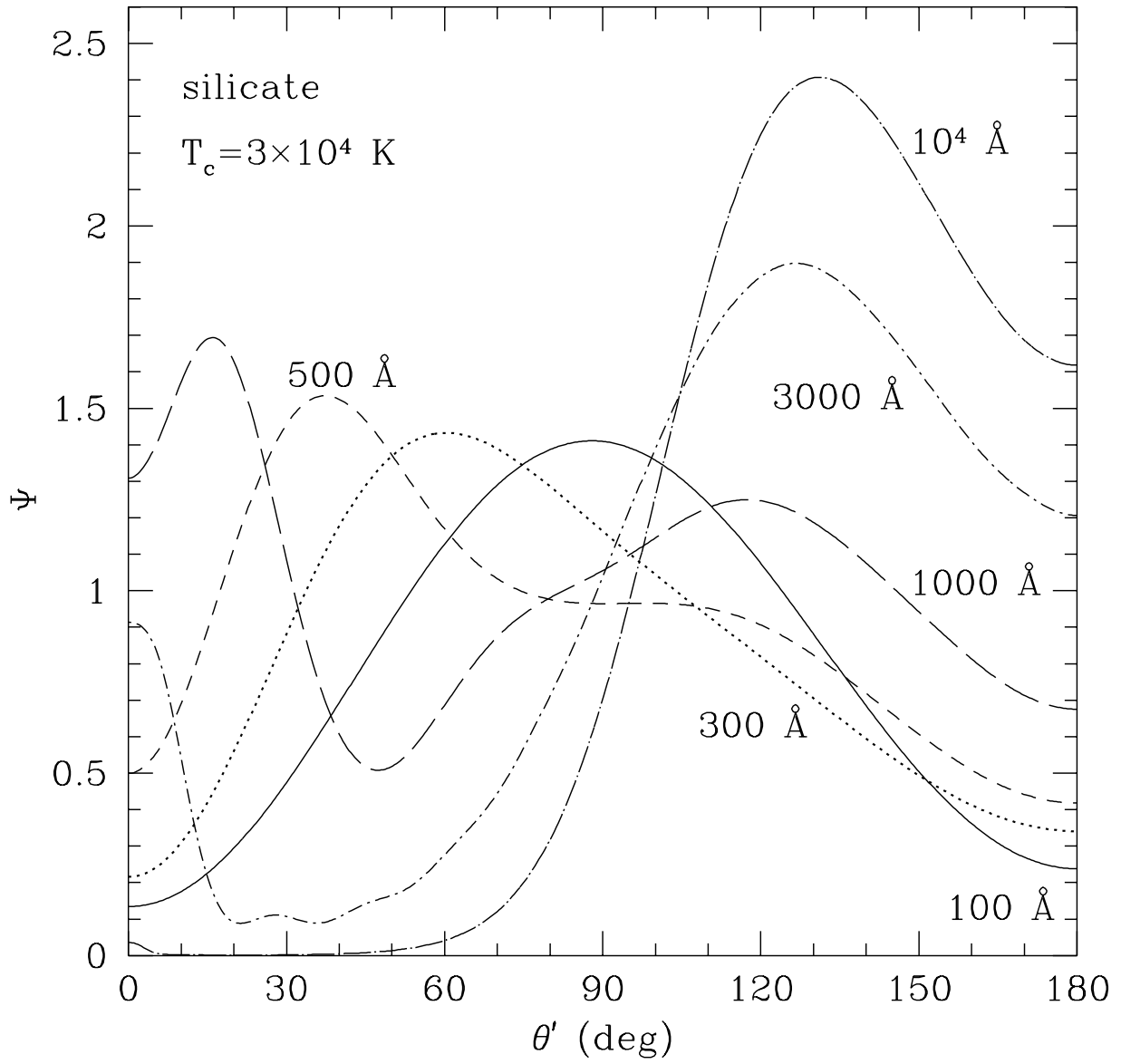


Fig. 8.— Same as fig. 7, but for silicate.

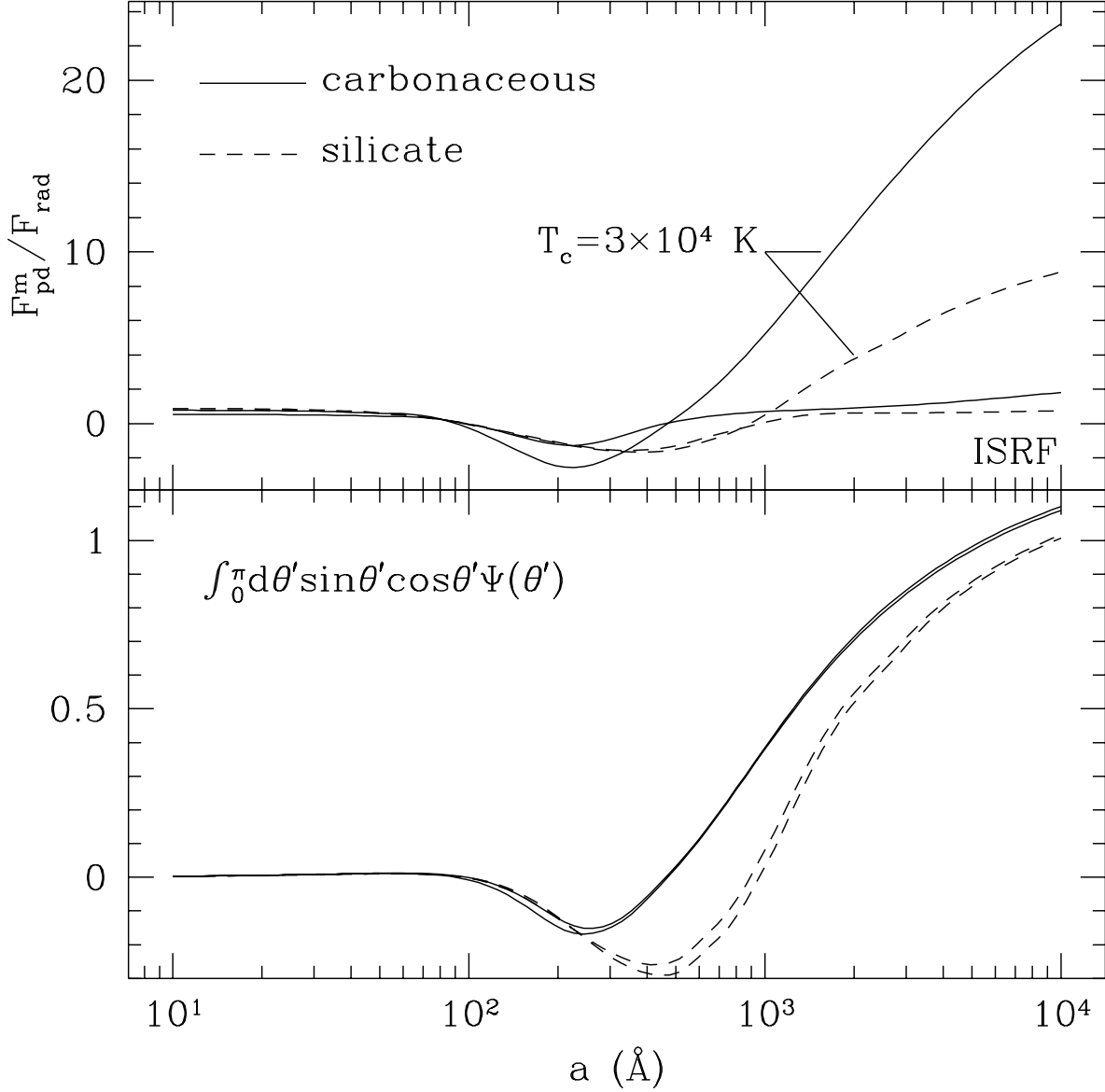


Fig. 9.— Lower panel: The photodesorption asymmetry integral appearing in the expression for the maximum possible force for flipping grains, F_{pd}^m (eq. 23). For carbonaceous (silicate) grains, the curve corresponding to a blackbody radiation field with $T_c = 3 \times 10^4 \text{ K}$ (cut off at 13.6 eV) lies below (above) that for the ISRF. Upper panel: Ratio of the maximum possible photodesorption force to the radiation pressure force, for parameter choices as indicated in Table 2 (note that E_{H_2} is not relevant here).

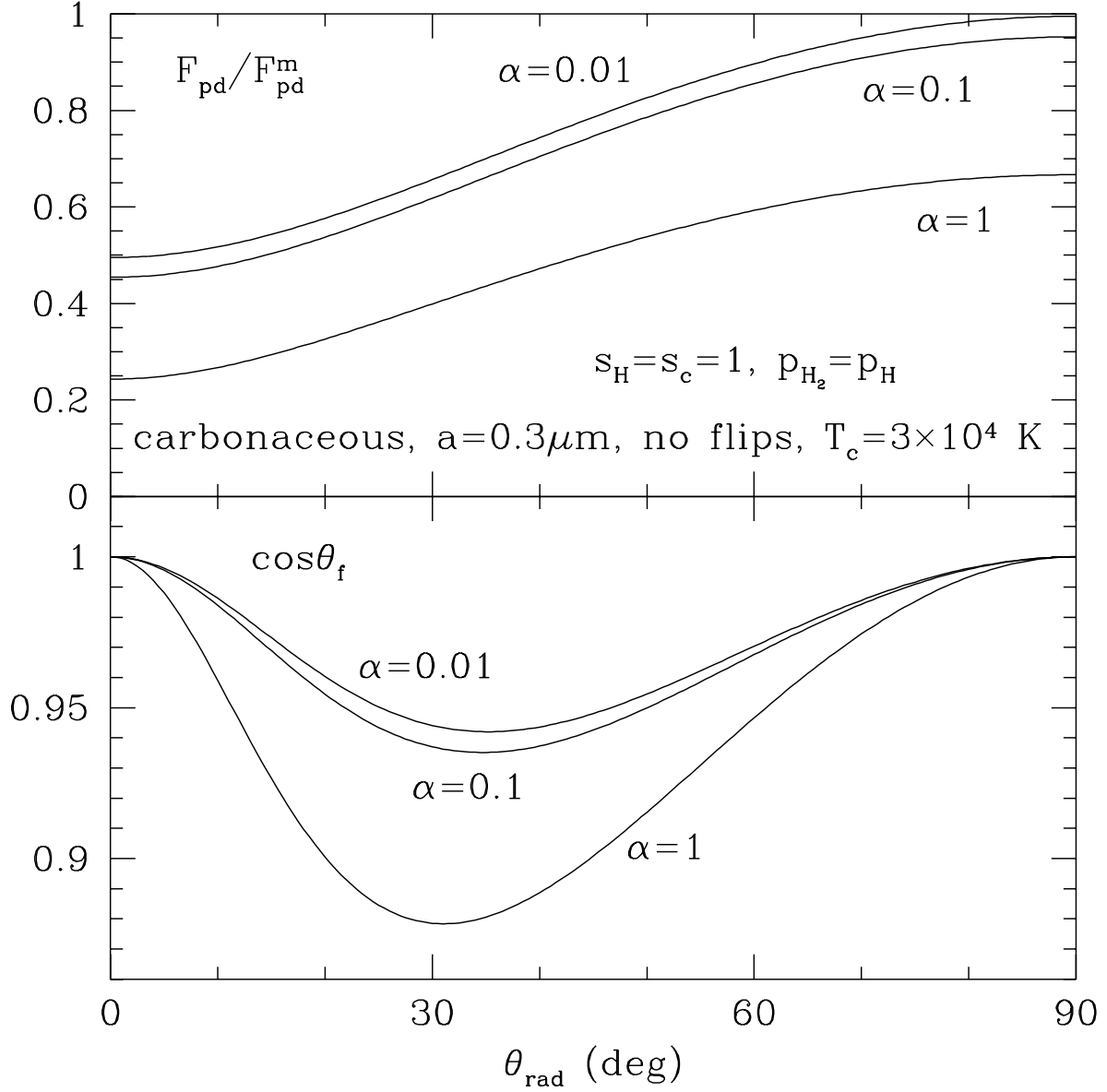


Fig. 10.— Upper panel: The photodesorption force as a function of angle θ_{rad} between $\hat{\omega}$ and \hat{S} , normalized to F_{pd}^m [see eq. (23)]. Lower panel: θ_f is the angle between \mathbf{F}_{pd} and \hat{S} .

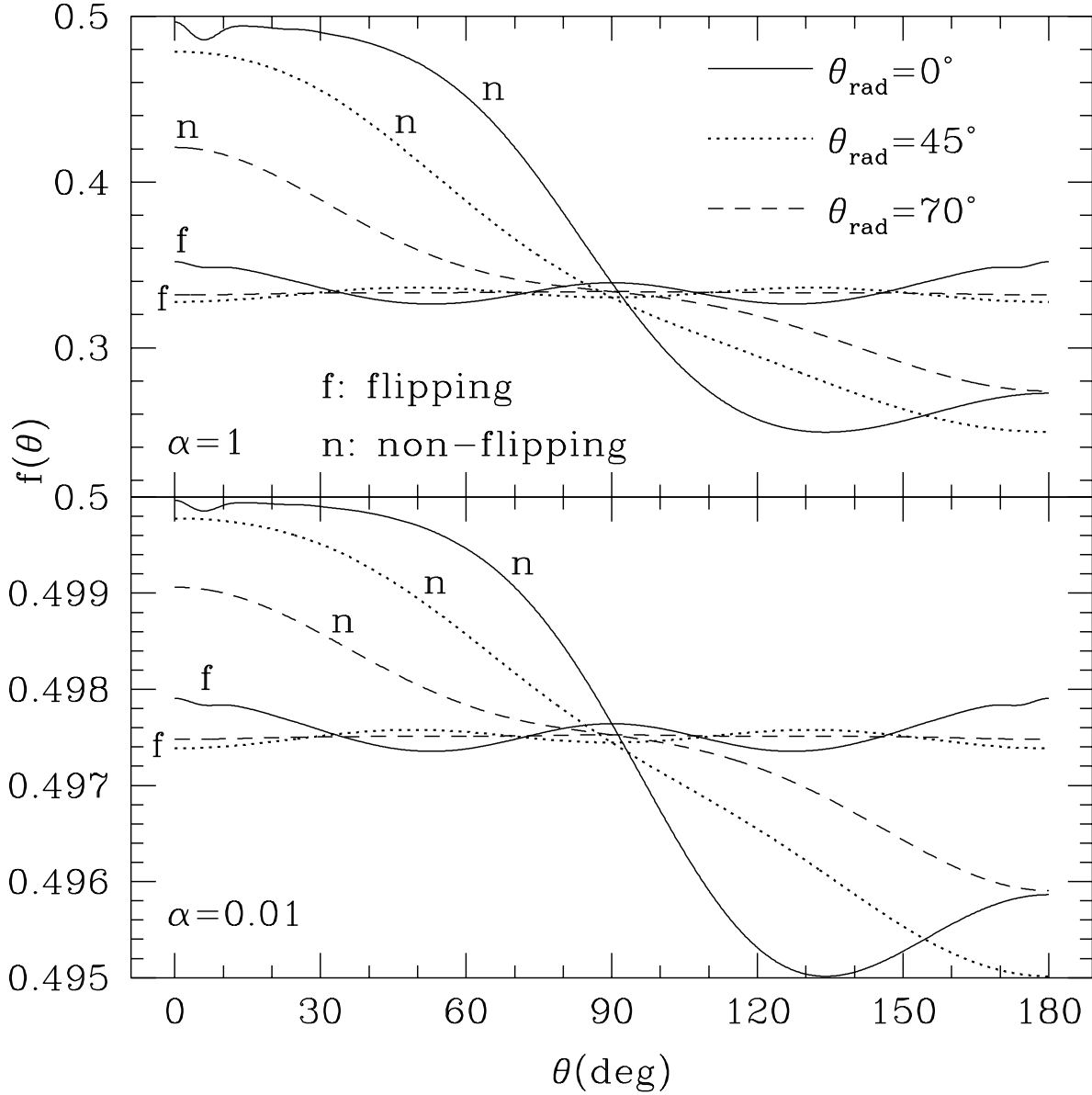


Fig. 11.— The occupation fraction f as a function of the angle θ with respect to the spin axis, for carbonaceous grains with $a = 0.3\mu\text{m}$, $s_{\text{H}} = s_{\text{c}} = 1$, $p_{\text{H}_2} = p_{\text{H}}$, a dilute blackbody radiation field with $T_{\text{c}} = 3 \times 10^4 \text{K}$, and two values of α : $\alpha = 0.01$ and $\alpha = 1$.

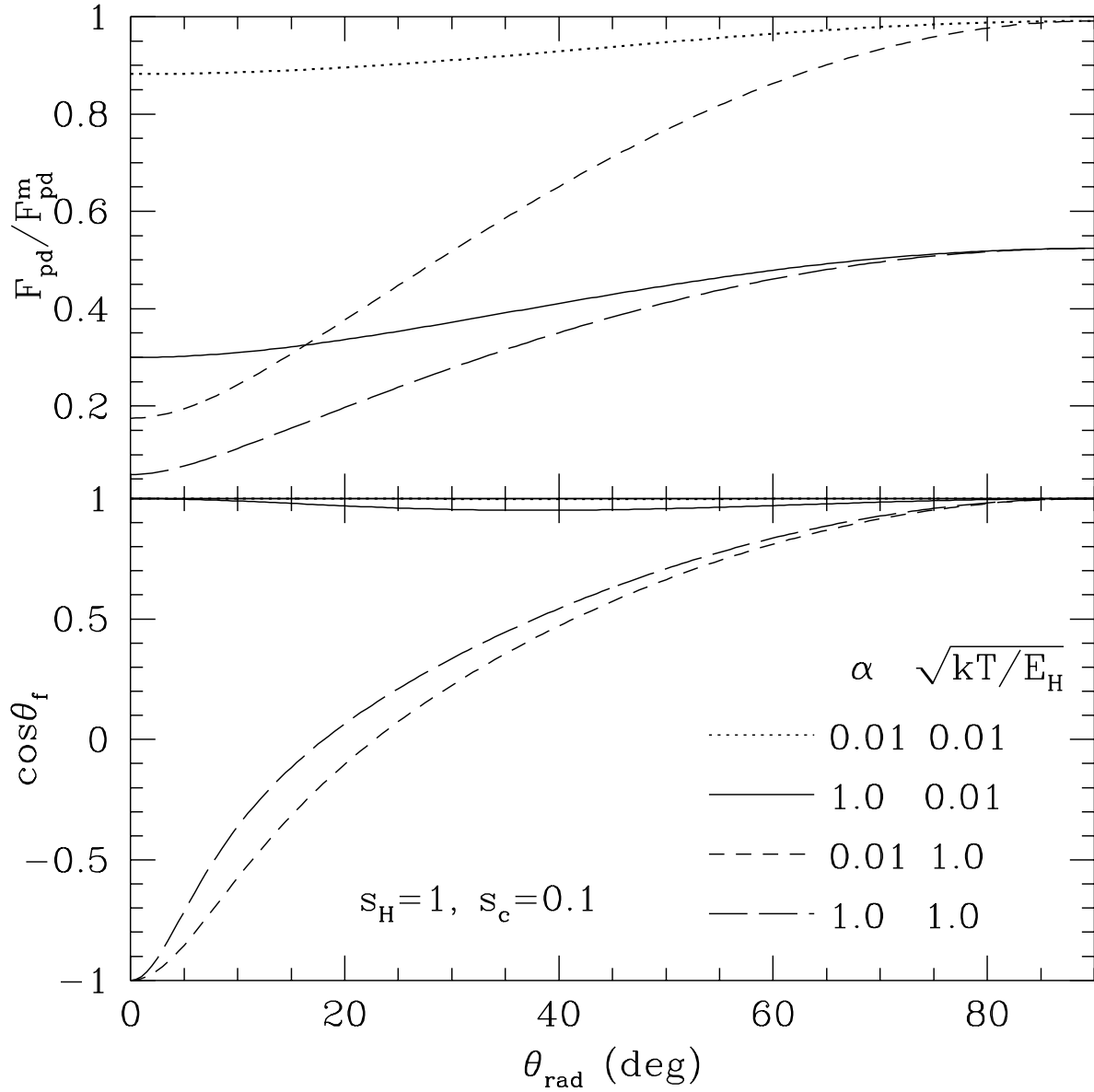


Fig. 12.— $F_{\text{pd}}/F_{\text{pd}}^{\text{m}}$ and $\cos \theta_f$ for non-flipping carbonaceous grains with $a = 0.3\mu\text{m}$, $s_{\text{H}} = 1$, $s_{\text{c}} = 0.1$, $p_{\text{H}_2} = p_{\text{H}}$, a blackbody radiation field with $T_{\text{c}} = 3 \times 10^4 \text{K}$, and various values of $(\alpha, \sqrt{kT/E_{\text{H}}})$.

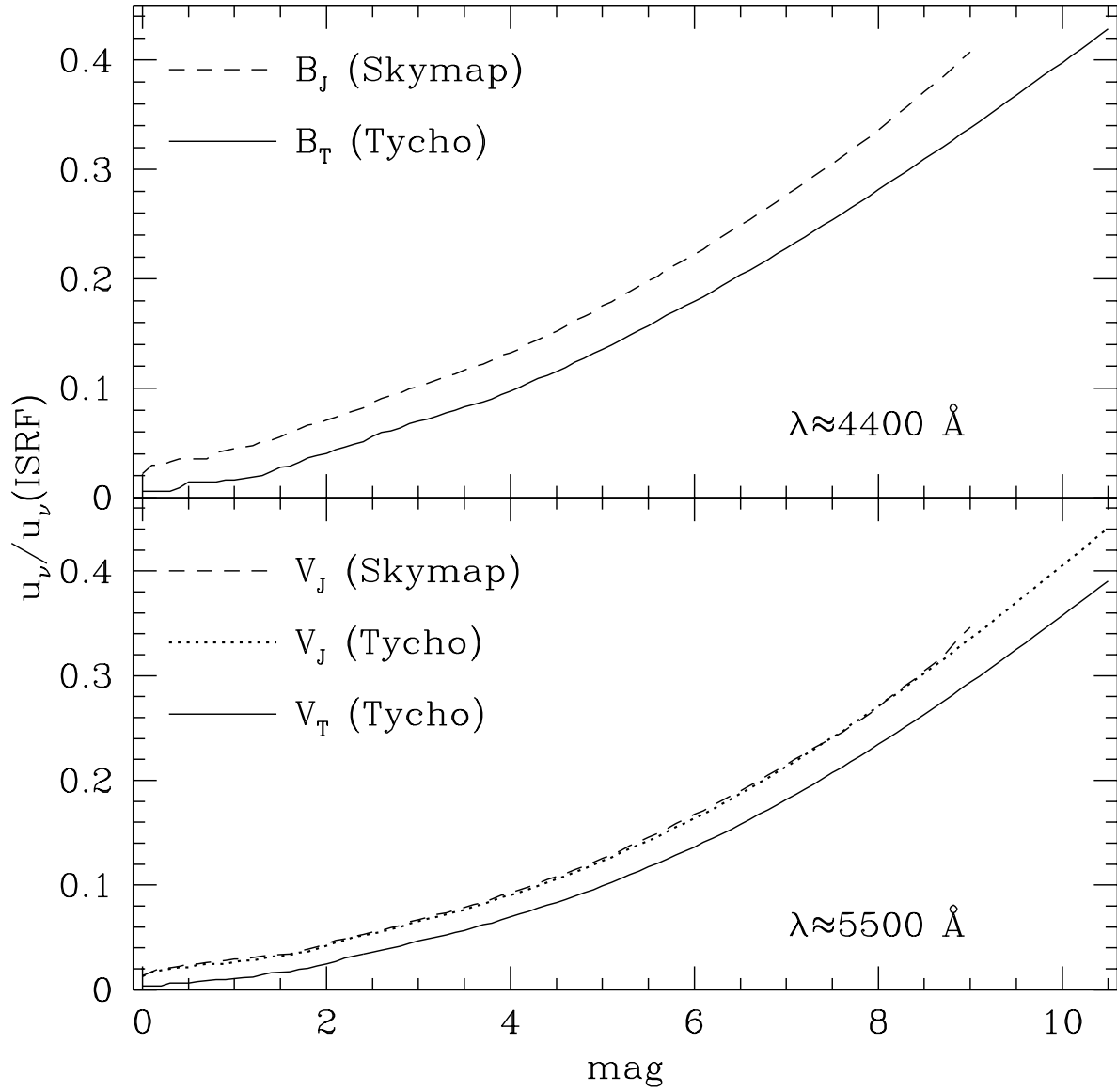


Fig. 13.— Energy density per wavelength interval, normalized to that of the ISRF, as a function of limiting magnitude. Results are from the Skymap and Tycho star catalogs. The Tycho fluxes are systematically low due to the absence of photometry for thousands of bright stars.

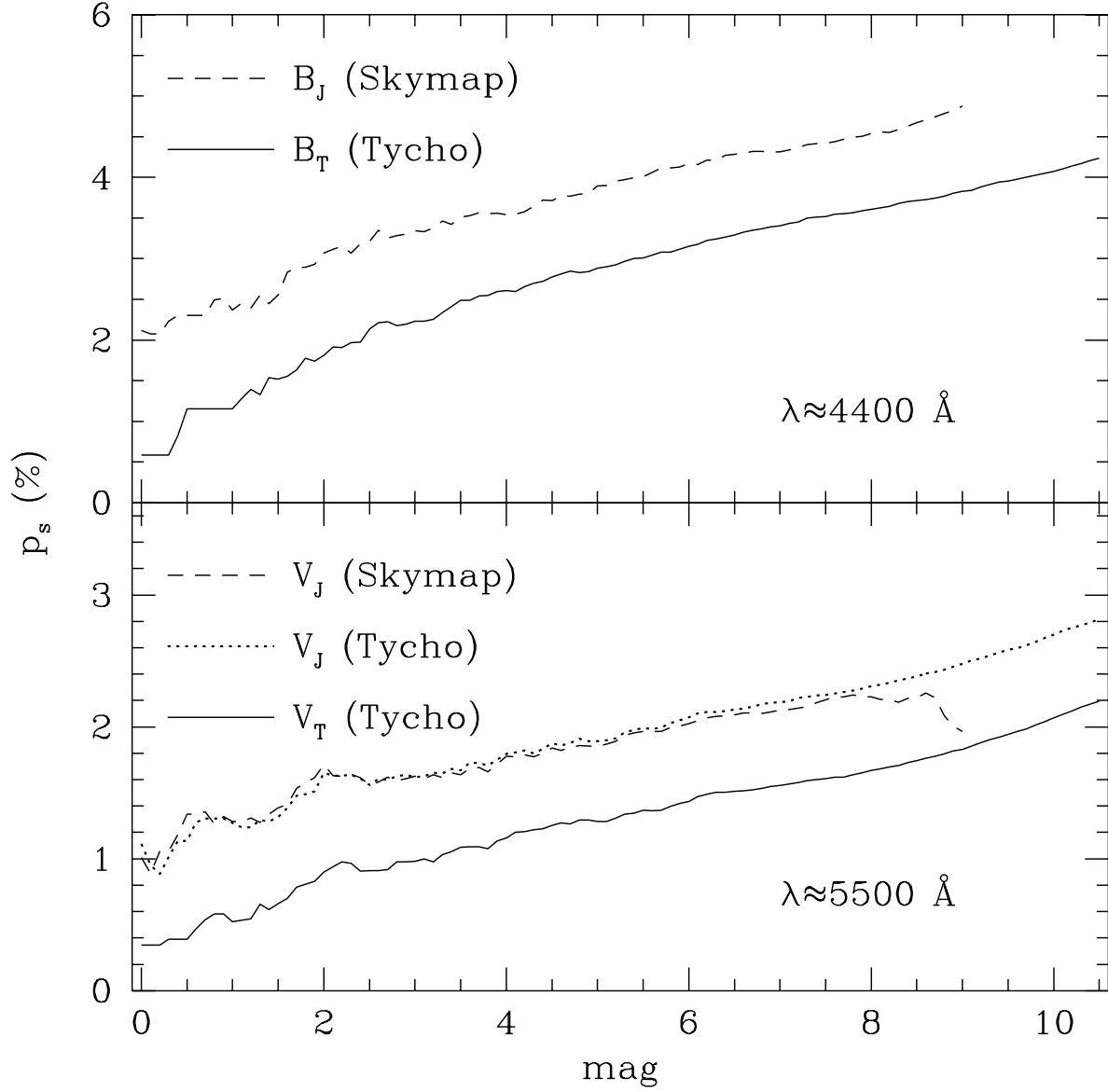


Fig. 14.— The normalized dipole moment p_s , i.e., the fraction of the energy density in the ISRF that is in the anisotropic component, as a function of limiting magnitude. The Tycho anisotropies are systematically low due to the absence of photometry for many of the brightest stars.

Table 1. Momentum Transfer Rates, Per Site

process	rate
photodesorption	$\frac{2}{3}R_{\text{pd}}p_{\text{H}}f$
H ₂ formation	$\frac{2}{3}R_{\text{arr}}^0s_{\text{c}}p_{\text{H}_2}f$
reflections	$[1 - s_{\text{H}} + f(s_{\text{H}} - s_{\text{c}})] \int_0^\infty dvP(v)n_{\text{H}}l^2v(2m_{\text{p}}v) = [1 - s_{\text{H}} + f(s_{\text{H}} - s_{\text{c}})] m_{\text{p}}R_{\text{arr}}^0\sqrt{\frac{\pi}{\beta}}$
sticking	$[s_{\text{H}} - f(s_{\text{H}} - s_{\text{c}})] \int_0^\infty dvP(v)n_{\text{H}}l^2v(m_{\text{p}}v) = [s_{\text{H}} - f(s_{\text{H}} - s_{\text{c}})] \frac{m_{\text{p}}R_{\text{arr}}^0}{2}\sqrt{\frac{\pi}{\beta}}$

Table 2. Canonical Photodesorption Parameters

parameter	symbol	value
photodesorption rate (graphite)	R_{pd}^0	$5 \times 10^{-10} G s^{-1}$
photodesorption rate (silicate)	R_{pd}^0	$2 \times 10^{-10} G s^{-1}$
kinetic energy of photodesorbed H	E_{H}	2 eV
kinetic energy of newly-formed H ₂	E_{H_2}	1 eV
surface site area	l^2	6 \AA^2
sticking probability	s_{H}	1
combination probability	s_{c}	1

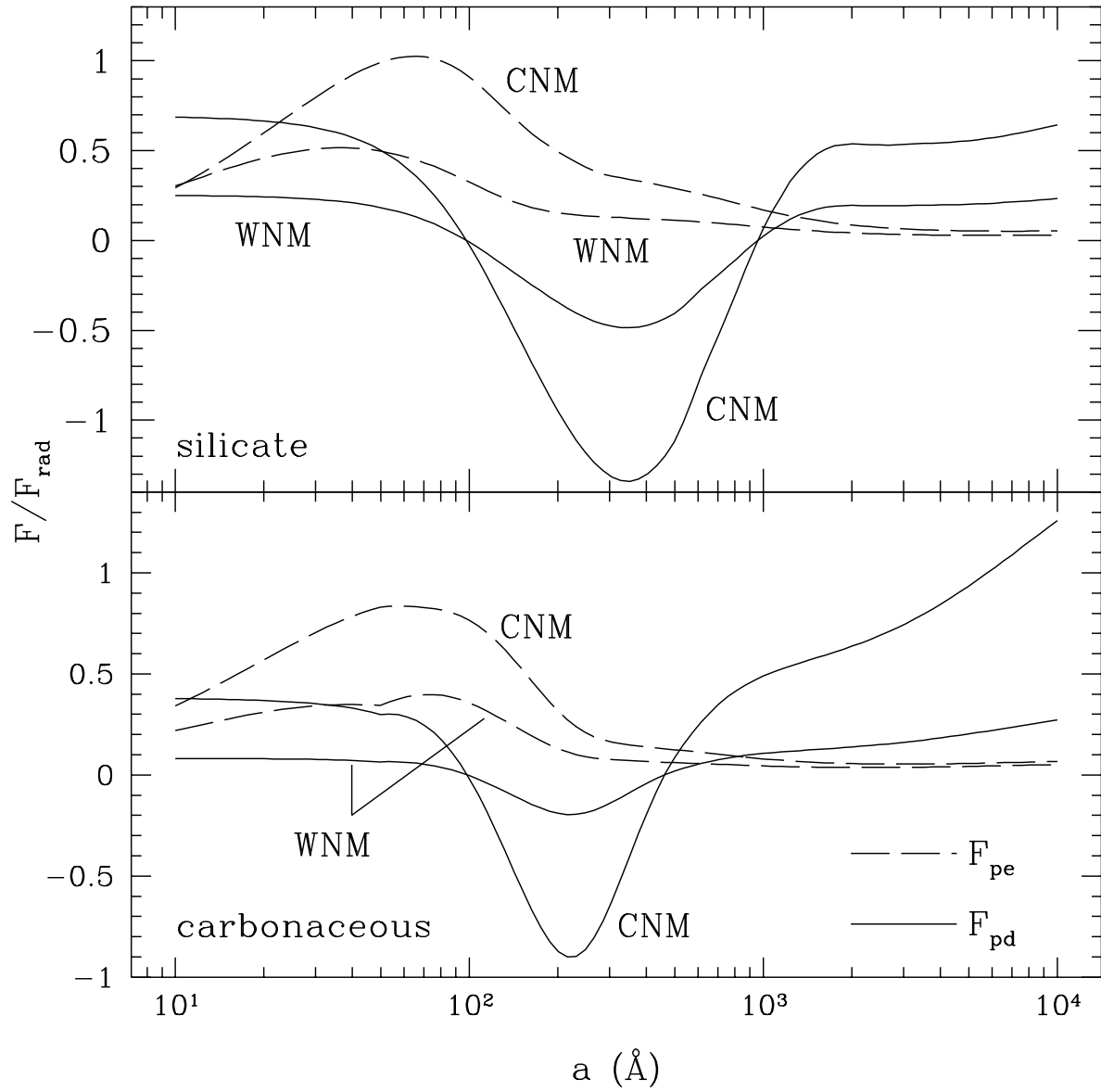


Fig. 15.— The photoelectric and photodesorption forces for grains in the warm and cold neutral media.

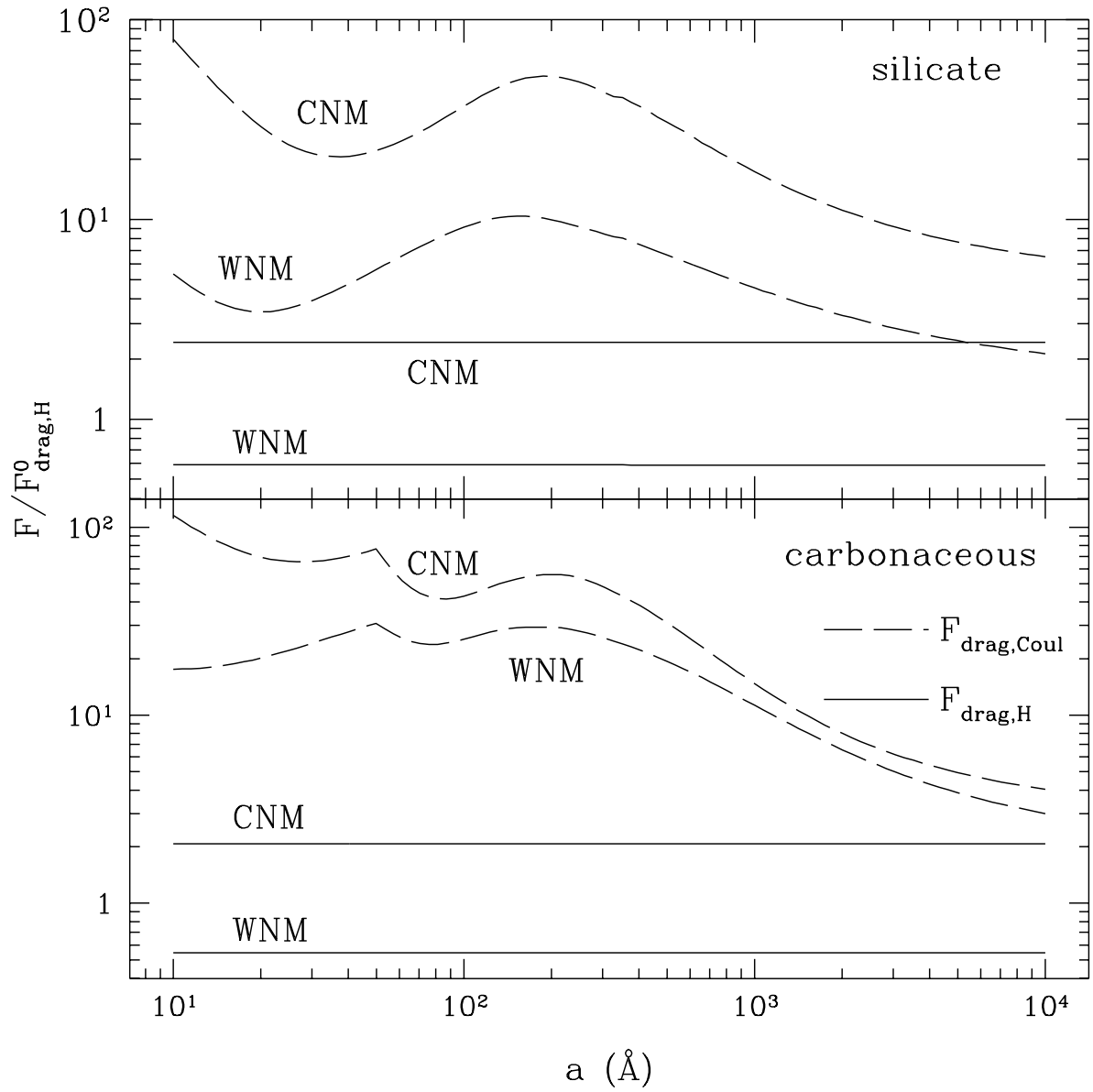


Fig. 16.— The drag forces due to collisions with neutral H and to Coulomb interactions with distant ions.

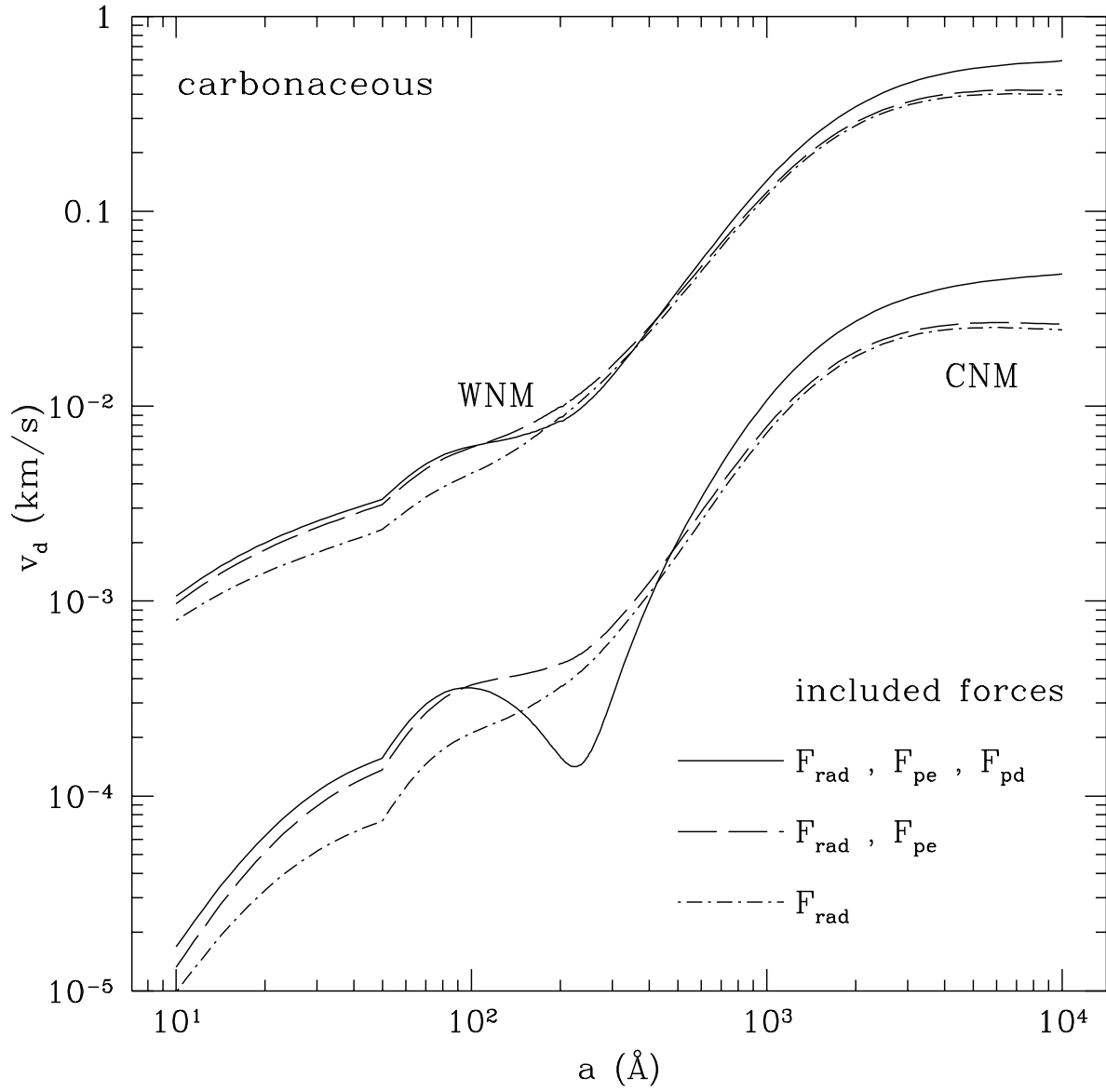


Fig. 17.— The drift speed for carbonaceous grains in the warm and cold neutral media.

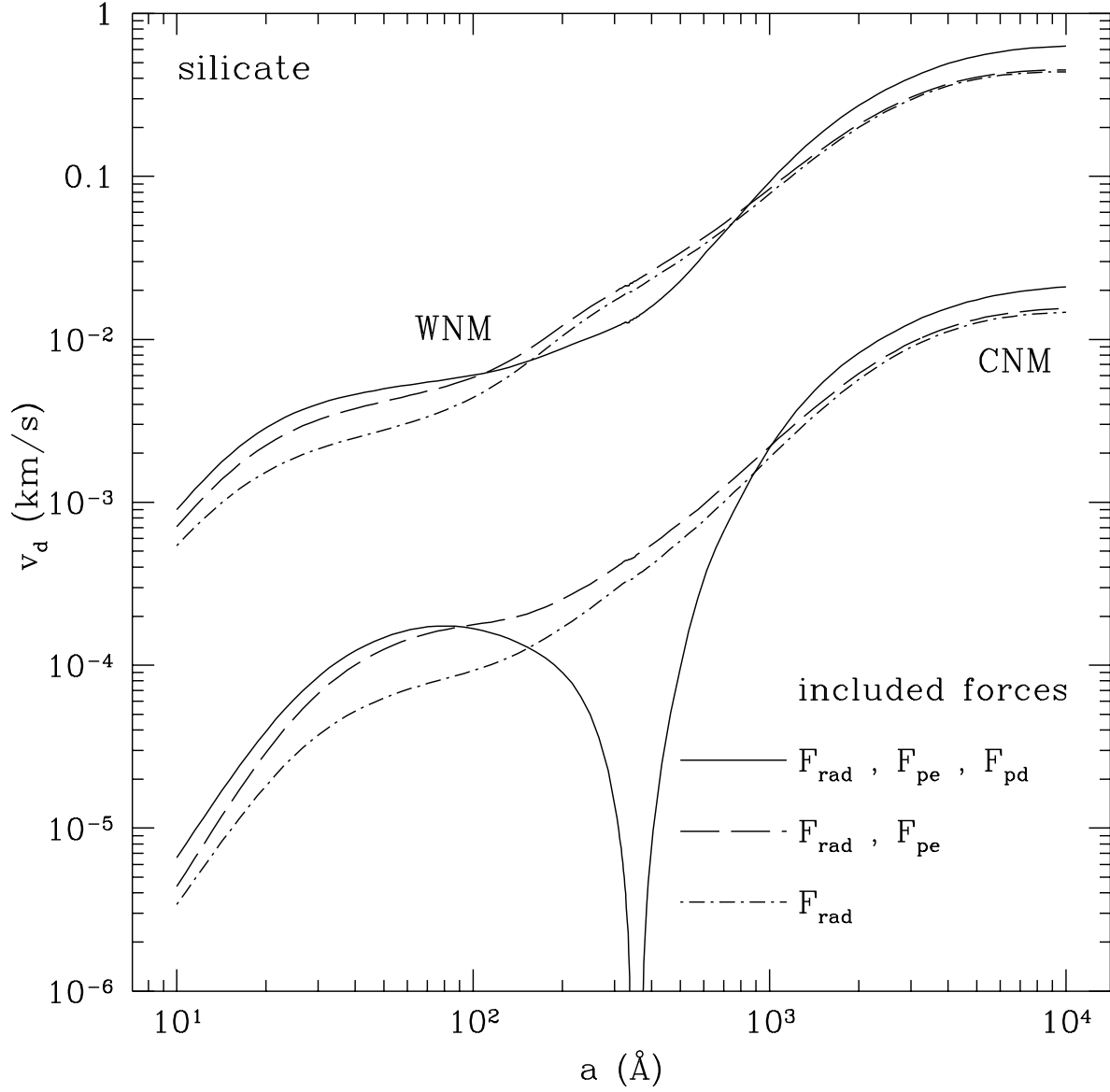


Fig. 18.— The drift speed for silicate grains in the warm and cold neutral media. Coincidentally, the minimum value of $F_{\text{rad}} + F_{\text{pe}} + F_{\text{pd}}$ in the CNM is very close to zero; hence the sharp drop in v_d when $a \approx 350$ Å.

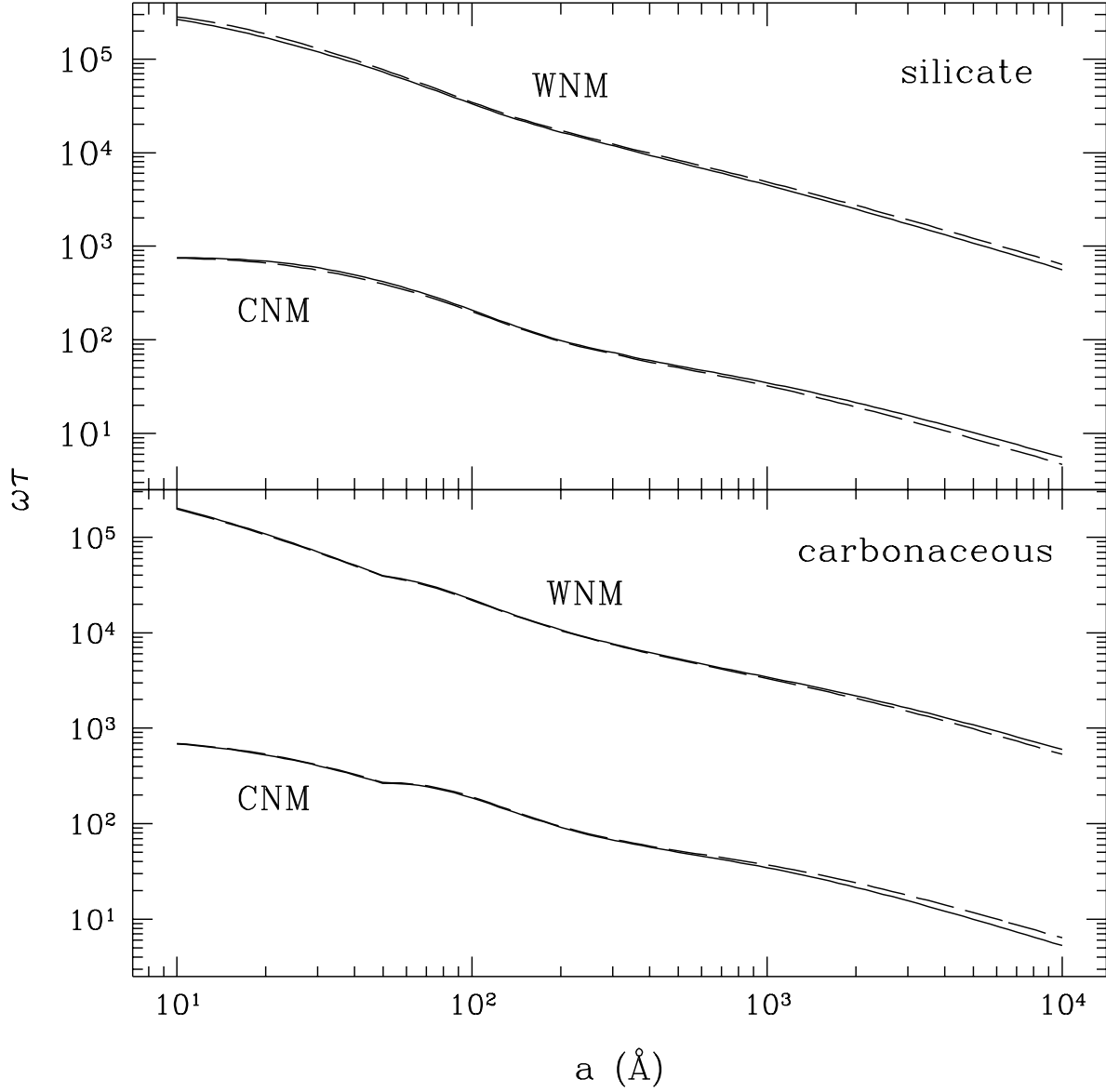


Fig. 19.— The product $\omega\tau$, where ω is the gyrofrequency for the charged grains in the ambient magnetic field, and τ is the drag time. Drift transverse to the magnetic field is suppressed by a factor $[1 + (\omega\tau)^2]^{1/2}$ [see eq. (37)].

Table 3. UV Energy Densities and Dipole Moments

Quantity	2740 Å	2365 Å	1965 Å	1565 Å
starlight dipole $(p_s \nu u_\nu)_*$ ^{a,b}	1.27	0.843	1.30	1.67
total starlight $(\nu u_\nu)_*$ ^{a,b}	4.43	3.23	4.73	5.27
total νu_ν ^{a,c}	4.90	5.47	6.47	6.90
ISRF νu_ν ^{a,d}	8.30	6.20	7.00	8.20
dipole/ISRF	0.152	0.136	0.185	0.205

^a 10^{-14} erg cm⁻³

^bGondhalekar 1989

^cGondhalekar et al. 1980

^dMathis et al. 1983

Table 4. Anisotropy Directions

Band	RA	dec	l	b
1565 Å	141°	-62°	281°	-8.2°
1965 Å	132°	-58°	275°	-8.9°
2365 Å	124°	-55°	270°	-10.5°
2740 Å	129°	-56°	273°	-9.3°
B	115°	-43°	257°	-9.8°
V	115°	-51°	264°	-13.6°

Note. — Celestial coordinates: right ascension (RA) and declination (dec); Galactic coordinates: longitude (l) and latitude (b).